

VIBRATORY RESPONSE OF DRY HUMAN SKULLS

by

Carmen L. McKnight

Submitted in partial fulfillment of the requirements
for the degree of Master of Applied Science

at

Dalhousie University
Halifax, Nova Scotia
March 2012

© Copyright by Carmen L. McKnight, 2012

DALHOUSIE UNIVERSITY

DEPARTMENT OF MECHANICAL ENGINEERING

The undersigned hereby certify that they have read and recommend to the Faculty of Graduate Studies for acceptance a thesis entitled “VIBRATORY RESPONSE OF DRY HUMAN SKULLS” by Carmen L. McKnight in partial fulfillment of the requirements for the degree of Master of Applied Science.

Dated: March 22, 2012

Research Co-Supervisors:

Readers:

DALHOUSIE UNIVERSITY

DATE: March 22, 2012

AUTHOR: Carmen L. McKnight

TITLE: VIBRATORY RESPONSE OF DRY HUMAN SKULLS

DEPARTMENT OR SCHOOL: Department of Mechanical Engineering

DEGREE: M.A.Sc.

CONVOCATION: May

YEAR: 2012

Permission is herewith granted to Dalhousie University to circulate and to have copied for non-commercial purposes, at its discretion, the above title upon the request of individuals or institutions. I understand that my thesis will be electronically available to the public.

The author reserves other publication rights, and neither the thesis nor extensive extracts from it may be printed or otherwise reproduced without the author's written permission.

The author attests that permission has been obtained for the use of any copyrighted material appearing in the thesis (other than brief excerpts requiring only proper acknowledgement in scholarly writing) and that all such use is clearly acknowledged.

Signature of Author

*To my parents, Carolyn and James McKnight, for their unwavering love,
support, and encouragement.*

TABLE OF CONTENTS

List of Tables	vii
List of Figures	viii
Abstract	x
List of Symbols Used	xi
Acknowledgements	xiv
Chapter 1 Introduction	1
Chapter 2 Literature Review	6
2.1 Bone Conduction	6
2.1.1 Air Conducted Sound versus Bone Conducted Sound	6
2.1.2 Conventional Bone Conduction versus Direct Bone Conduction	7
2.1.3 Linearity	8
2.1.4 Resonant Frequencies	9
2.1.5 Lateralization	9
2.1.6 Transcranial Attenuation	10
2.1.7 Wave Propagation in Skull Bone	11
2.2 Lamb Waves	13
2.3 Spherical Shells	20
2.4 Measurement Techniques	23
2.4.1 Contact Measurement Devices	23
2.4.2 Non-Contact Measurement Devices	23
2.4.3 Laser Doppler Vibrometry	23
Chapter 3 Experimentation	28
3.1 Experiment 1	29
3.1.1 Skull Prep	29

3.1.2	Setup	30
3.1.3	Preliminary Post-Processing	32
3.2	Experiment 2	33
3.2.1	Skull Prep	33
3.2.2	Setup	34
3.2.3	Preliminary Data Post-Processing	40
3.3	Experiment 3	41
3.3.1	Skull Prep	41
3.3.2	Setup	41
3.3.3	Preliminary Post-Processing	43
Chapter 4	Results and Discussion	44
4.1	3D Vibration Patterns	44
4.2	Wave Propagation in Skull Bone	47
Chapter 5	Conclusions	61
References	63
Appendix A	Force and Admittance Calculation - MATLAB® Code	66
Appendix B	Visual Basic® Macros	74
Appendix C	Experiment 2 Data Analysis	81
Appendix D	Constrained, Non-Linear Least Squares Optimization Scheme	86

LIST OF TABLES

2.1	Average Skull Parameters	22
3.1	Experiment 1: Acquisition Settings	30
3.2	Experiment 1: Channel Settings	31
3.3	Experiment 1: Channel Range Settings for Acceleration Measurement	32
3.4	Experiment 2: 3D Alignment Quality for Skull A	38
3.5	Experiment 2: 3D Alignment Quality for Skull B	38
3.6	Experiment 2: Acquisition Settings	39
3.7	Experiment 2: Channel Settings	39
3.8	Experiment 3: Settings	42
4.1	Geometric and Material Fitting Parameters	60

LIST OF FIGURES

1.1	Prevalence of Hearing Loss by Age Group and Gender	1
1.2	Gross Anatomy of the Human Ear	2
1.3	Sound Transmission through Bone Conduction	3
1.4	Cochlear Limited’s Baha®	4
1.5	Surgical Placement of a Baha®	4
2.1	Plate	13
2.2	Zero-Order Lamb Wave Modes	19
2.3	Spherical Shell Model	22
2.4	Schematic of a Laser Doppler Vibrometer (LDV)	24
2.5	Polytec’s 3D Single Point Laser Doppler Vibrometer (LDV)	26
2.6	Polytec’s 3D Scanning Laser Doppler Vibrometer (LDV)	27
3.1	Dry Human Skulls	28
3.2	Elastic Suspension System	29
3.3	Experiment 2: Measurement Views	34
3.4	Experiment 2: Wiring Diagram	35
4.1	Experiment 2: 3D Velocity Field for Skull A	45
4.2	Experiment 2: 3D Velocity Field for Skull B	46
4.3	Experiment 2: 2D Velocity Field at 16000 Hz	47
4.4	Force Comparison	48
4.5	Experiment 1: Input Force	49
4.6	Experiment 1: Admittance Data	51
4.7	Experiment 1: Admittance of Skull A with and without Mandible Attached	52
4.8	Experiment 1: Mode Number versus Resonant Frequency	53
4.9	Experiment 2: Dispersion Relationship	55

4.10	3D Velocity Field at 10550 Hz	56
4.11	Experiment 3: Phase Difference	57
4.12	Experiment 3: Coherence	57
4.13	Experiment 3: H2 Frequency Response Function	58
4.14	Experiment 2: Dispersion Relationship Fit to Spherical Shell Model	59
C.1	3D Velocity Field at 10550 Hz	82
C.2	Normal and Tangential Components of Surface Velocity	82
C.3	Contour Plots of Normal Surface Velocity	84

ABSTRACT

Hearing loss affects millions of people of all ages and is commonly treated with hearing aids and prostheses. Bone anchored hearing prostheses use bone conduction to transmit sound through the skull bone to the functioning inner ear and cochlea, bypassing the outer and middle ear. A challenge associated with these prostheses is optimizing the location of the surgical implant. A better understanding of how vibrations travel through the skull bone will be beneficial in the improvement of current prostheses and the development of new bone conduction technologies.

Using laser Doppler vibrometry, vibration characteristics of dry human skulls were investigated. Three-dimensional vibration patterns were obtained at several frequencies and the dispersion relationship was determined. A closed-spherical shell model proved to be a good indicator of the frequency response of a dry human skull in the frequency range of normal human hearing.

LIST OF SYMBOLS USED

Roman symbol	Description	Units
A	instantaneous amplitude	m
A_o	peak amplitude	m
AP	auto power spectra	-
c_1	longitudinal wave velocity	m/s
c_2	transverse wave velocity	m/s
COH	coherence function	-
CP	cross power spectra	-
E	Young's modulus	Pa
f	frequency	s^{-1}
f_b	Bragg cell frequency shift	s^{-1}
f_d	Doppler frequency shift	s^{-1}
F	Force	N
G	shear modulus	Pa
h	thickness	m
H1,H2	frequency response functions	-
k	wave number	m^{-1}
m_b	effective mass of Baha [®]	kg
r	radius	m
R^2	goodness of fit value	-
R_1	reference channel 1	-
R_2	reference channel 2	-
R_3	reference channel 3	-
S	spectrum	-
t	time	s
u, v	displacement functions	-
v_g	group velocity	m/s
v_l	linear velocity	m/s
v_p	phase velocity	m/s

Roman symbol	Description	Units
$v_{p,a}$	antisymmetric Lamb wave phase velocity	m/s
$v_{p,s}$	symmetric Lamb wave phase velocity	m/s
v_s	surface velocity	m/s
V	vibrometer channel	-

Greek symbol	Description	Units
α	longitudinal wave number	m^{-1}
β	transverse wave number	m^{-1}
κ	$\kappa = \frac{c_1^2}{c_2^2} = \frac{\lambda+2\mu}{\mu}$	-
λ	wavelength	m
λ_l, μ_l	Lamé elastic coefficients	Pa
λ_n	$\lambda = n(n+1)$	-
n	mode number	-
ν	Poisson's ratio	-
ρ	density	kg/m^{-3}
σ_{ij}	stress tensor	Pa
ϕ	phase	°
ϕ_o	phase offset	°
φ	scalar potential function	-
ψ_z	vector potential function	-
ω	angular frequency	rad/s
Ω	dimensionless frequency	-

ACKNOWLEDGEMENTS

Foremost, I would like to thank my supervisors Dr. Darrel A. Doman and Dr. Jeremy A. Brown. Dr. Doman provided mentorship, guidance and encouragement while keeping me grounded. Dr. Brown offered support and direction, and gave me the chance to work with state-of-the-art equipment in the S.E.N.S.E. Laboratory. I greatly appreciate the opportunities made available by my supervisors throughout this degree.

I am indebted to Dr. Robert B. Adamson for his time and patience. His knowledge and expertise have been invaluable.

To the members of the S.E.N.S.E. Laboratory and the T Building; thank you for giving me not one but two welcoming and supportive work environments. Your insights, friendships and laughter kept me going. It was a pleasure working with all of you.

The financial support I received from the Natural Sciences and Engineering Research Council of Canada helped make this research project possible.

Lastly, to all my family and friends, especially my parents, Carolyn and James McKnight, and my dear friend, Katherine Malec, for always believing in me and supporting me in all my endeavours. I don't know what I would do without you.

CHAPTER 1

INTRODUCTION

Hearing impairment is caused by a variety of congenital and environmental factors and, though more prevalent in the elderly population, affects people of all ages (Figure 1.1).

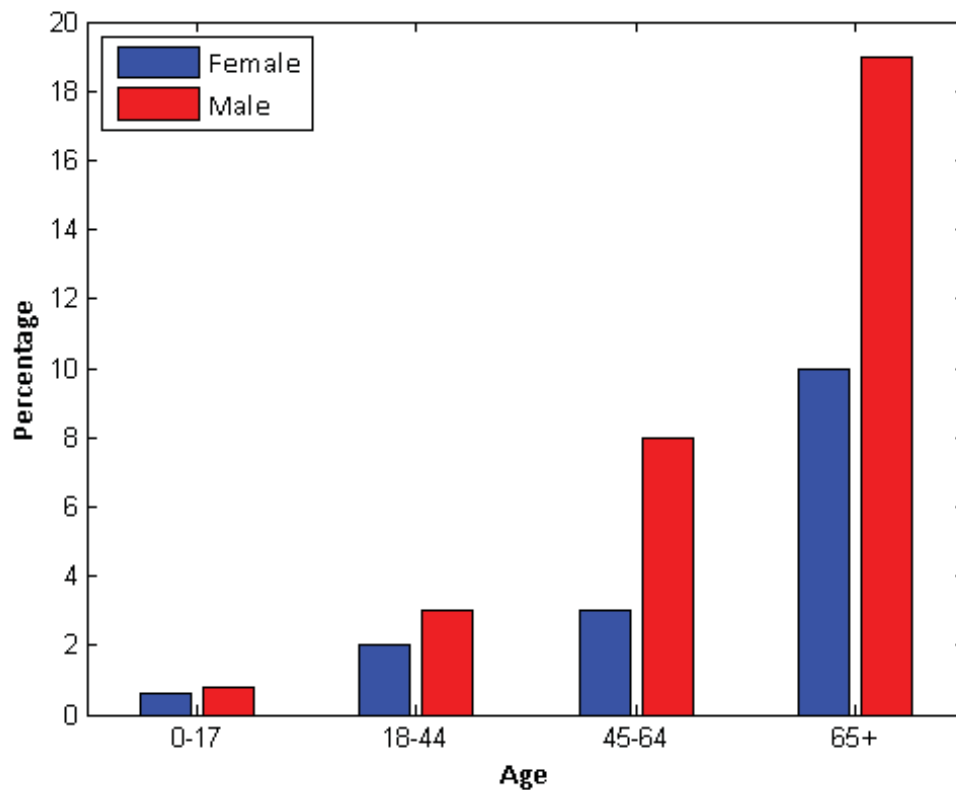


Figure 1.1: Prevalence of hearing loss by age group and gender. Adapted from O'Neill *et al.* (1999).

There are two fundamental types of hearing loss. Sensorineural hearing loss is caused by defects in the inner ear or acoustic nerve, while conductive hearing loss occurs when defects are present in the outer or middle ear. A third type of hearing impairment is a combination of sensorineural and conductive hearing loss and is referred to as mixed hearing loss. Figure 1.2 is an illustration of the gross anatomy of the ear and indicates the outer, middle and inner ear regions. Often, hearing aids (amplification of sound) and prostheses (transmission of sound) are effective treatments for these conditions.

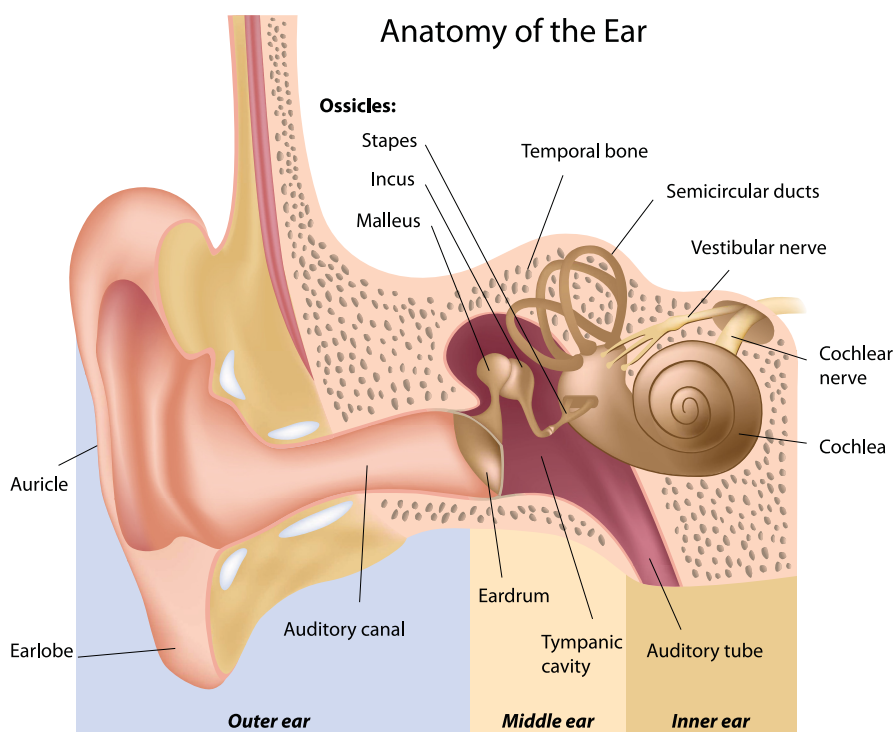


Figure 1.2: Gross anatomy of the human ear including the outer, middle and inner ear.

People with normal auditory function perceive sound primarily through air conduction, where sound pressures propagate through the air in the external auditory canal and vibrate the ear drum or tympanic membrane. This in turn causes motion of the malleus, the incus and, eventually, the stapes, which ultimately creates pressure waves in the cochlear fluid. Figure 1.3 illustrates how a bone conducted sound ultimately reaches the inner ear. Mechanical vibrations generated by a bone anchored hearing prostheses embedded in the temporal bone of the skull are transmitted through the skull bone directly to the cochlea, bypassing the outer and middle ear.

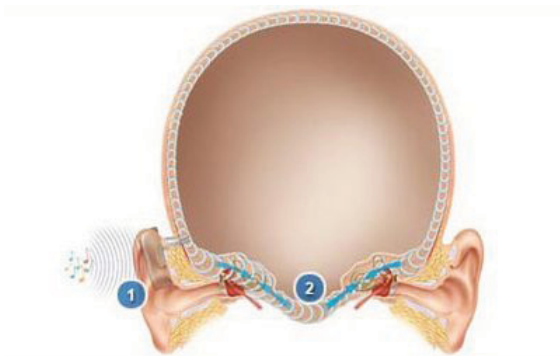


Figure 1.3: Schematic of bone conducted sound transmission through the skull bone to the cochlea. The outer and middle ear are bypassed. Picture taken from Cochlear Ltd. (2011).

An example of a bone conducted sound is the psychoacoustic perception of one's voice when the ear is occluded. Bone anchored hearing prostheses utilize bone conduction to treat conductive hearing loss, mixed hearing loss and single-sided deafness, where conventional hearing aids may not be effective. These prostheses are a successful and widely used treatment with more than 50,000 prostheses implanted world wide (Cochlear Ltd., 2011) in both children and adult patients since they were first invented in 1977 (Tjellström *et al.*, 1983). Two examples of commercially available bone anchored hearing prostheses are Cochlear Limited's Baha[®] and Oticon Medical's Ponto[™]. Figure 1.4 is an exploded view of a Baha[®], indicating the three major components; (1) sound processor, (2) external abutment and (3) titanium implant.

Sound waves are picked up by a microphone and converted into an electrical signal, which is filtered and amplified by the sound processor. A vibrating transducer converts this electrical signal into a mechanical vibration, which is transmitted through the external abutment to the titanium implant, and ultimately to the skull bone. The titanium implant is surgically embedded behind the ear in the temporal bone of the skull. Figure 1.5 shows the external abutment protruding out from the skin. The sound processor is not attached until 3–4 months after the initial surgery to ensure the skull bone has fully osseointegrated with the titanium implant (Tjellström *et al.*, 2001). The inset in Figure 1.5 shows a fully functioning Baha[®] with the sound processor attached.

The placement of bone anchored hearing prostheses are surgically limited by the thickness of the temporal bone (Tjellström *et al.*, 2001). Future bone conducted hearing technologies that do not suffer from this surgical limitation may realize improved sound quality with

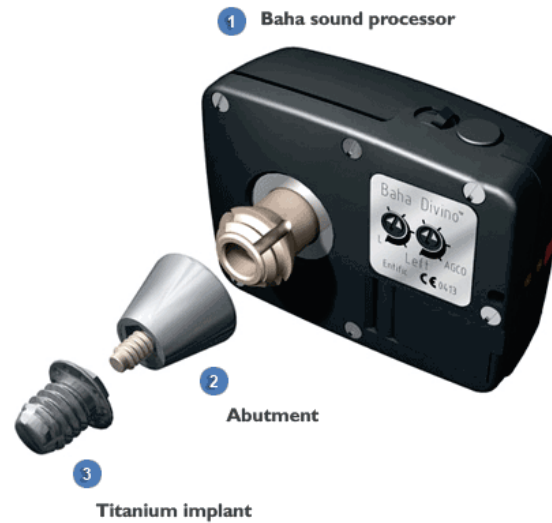


Figure 1.4: Exploded view of Cochlear Limited's Baha[®]. Three major components; (1) sound processor, (2) external abutment and (3) titanium implant. Picture taken from Cochlear Ltd. (2011).



Figure 1.5: Illustration of the surgical placement of a Baha[®]. The external abutment can be seen protruding out from the skin. The inset figure shows the fully functioning Baha[®] with the sound processor attached. Picture taken from Cochlear Ltd. (2011).

the optimization of device location on the skull. Thus, a thorough understanding of bone conduction mechanisms is required, however this has yet to be achieved (Stenfelt *et al.*, 2000; Eeg-Olofsson *et al.*, 2008). In terms of wave propagation in the skull, there is significant debate in the literature (Stenfelt & Goode, 2005a), which centers around two major theories; Lamb plate waves and spherical shell models. These theories are discussed in detail in Chapter 2. The purpose of this work is to study the vibratory response of human skull bone through experimental testing in order to gain a better understanding of bone conduction. Understanding the transmission mechanisms of bone conducted sound will ultimately aid in making improvements to current prostheses and developing new bone conduction hearing technologies.

A review of the literature will follow in Chapter 2. Chapter 3 will discuss the experimental methods used. The results and a discussion of the findings is given in Chapter 4. Concluding remarks and recommendations will presented in Chapter 5. A full list of symbols used is included on page xi for the reader's convenience.

CHAPTER 2

LITERATURE REVIEW

The following chapter first provides a review of the literature on bone conduction. Lamb plate theory and a closed spherical shell model are then discussed. Finally, an outline of measurement techniques is given with an extensive discussion on laser Doppler vibrometry.

2.1 Bone Conduction

2.1.1 *Air Conducted Sound versus Bone Conducted Sound*

One of the first questions to be addressed concerning bone conducted sound was whether or not the cochlea was the organ being stimulated. The first to investigate this was von Békésy, who endeavoured to subjectively cancel a bone conducted sound with an air conducted sound (source: Stenfelt & Goode (2005a)). If a bone conducted sound stimulates the cochlea, then a air conducted sound of the same signal and amplitude but 180° out phase should cancel out the bone conducted sound resulting in no sound perception. Von Békésy sucessfully cancelled a bone conducted stimulus with an air conducted stimulus in one subject at a single frequency (source: Stenfelt & Goode (2005a)). Following this finding, several studies measured the cochlear microphonic in cats (source: Stenfelt & Goode (2005a)). The cochlear microphonic is an electrical potential generated by the hair cells in the cochlea in response to an acoustic stimulus. The signals from the air and bone stimuli were found to be similar giving further credence to von Békésy's initial hypothesis. Later experiments by Khanna *et al.* (1976) subjectively cancelled an air conducted sound

with a bone conducted sound at a single frequency over a range of hearing levels. The physical vibration of the basilar membrane was found to be similar for air and bone conducted sounds by von Békésy (1955), who showed that waves travel from the base of the basilar membrane to the apex, regardless of the stimulation location of the bone conducted stimulus on the cochlea. Furthermore, laser Doppler vibrometry experiments conducted by Stenfelt *et al.* (2003) on the basilar membrane showed similar vibratory responses. This ample experimental evidence proves that on the cochlear level, there is no perceived difference between an air conducted sound and a bone conducted sound. Therefore, the mechanisms by which vibrations reach the cochlea are of interest when considering bone conducted sound.

2.1.2 *Conventional Bone Conduction versus Direct Bone Conduction*

The distinction between conventional bone conduction and direct bone conduction is that conventional bone conduction stimulates the skull via the skin and subcutaneous soft tissues, whereas direct bone conduction stimulates the skull directly. Conventional bone conduction was used in early bone conduction hearing prostheses. However, since the mid to late 1980s, direct bone conduction hearing prostheses, such as Cochlear Limited's Baha[®] and Oticon Medical's Ponto[™], have been the preferred clinical treatment for conductive hearing loss, mixed hearing loss and single-sided deafness.

Håkansson *et al.* (1984) conducted hearing threshold experiments on subjects fitted with direct bone conduction hearing prostheses and compared these thresholds with those of conventional bone conduction hearing prostheses. Their study found hearing thresholds to be considerably lower, approximately 10–20 dB for a frequency range of 600–6000 Hz, when using direct bone conduction as opposed to conventional (Håkansson *et al.*, 1984). These findings were confirmed by a later study that found in order to produce an equivalent hearing sensation, a lower stimulation velocity is required for vibrators that penetrate the skin and are rigidly fix to the skull, than for those that are coupled to the skin (Håkansson *et al.*, 1986). These results demonstrated the many benefits of the, then new, Baha[®] hearing prosthesis. Among these benefits are less distortions and lower power consumption, which allows for all the electronics to be contained in a single, small housing (Håkansson *et al.*, 1984, 1986).

Håkansson *et al.* (1986) compared the differences between mechanical point impedances *in vivo* for both conventional and direct BC stimulation. They concluded that previous mechanical point impedances of the human head that had been measured using conventional bone conduction were in fact a measurement of both the skin and subcutaneous soft tissues that cover the skull (Håkansson *et al.*, 1986). This skin impedance is not only dependent on the properties of the skin and subcutaneous soft tissues but also of the coupling between the skin and the impedance head (Håkansson *et al.*, 1986).

2.1.3 Linearity

A cancellation study conducted by Khanna *et al.* (1976) that used a conventional bone conduction stimulus found distortions in the form of a second harmonic at frequencies below 2000 Hz. They proposed that this distortion was caused by either an imperfect elastic coupling between the vibrator and the skin or by the asymmetric nature of the cochlear response (Khanna *et al.*, 1976). These findings are consistent with those of a later study conducted by Arlinger *et al.* (1978) who also utilized conventional bone conduction. They found the propagation of bone conducted sound to be of a non-linear nature and attributed this finding to the non-linear behaviour of the bone tissue of the human skull (Arlinger *et al.*, 1978).

Håkansson *et al.* (1996) conducted *in vivo* experiments on a subject with bilateral abutments implanted into the skull bone to test for non-linearities in sound transmission. No indications of non-linear behaviour were reported. They suggested that differences between their study, and the findings of Khanna *et al.* (1976) and Arlinger *et al.* (1978) were due to the methodology used. Since conventional bone conduction was used as a stimulus in the latter two studies, the result was an indirect measurement of the input signal onto the skull bone (Håkansson *et al.*, 1996). This is consistent with previous work discussed earlier that suggests mechanical point impedance measurements taken using conventional bone conduction is actually a measure of the skin impedance and not of the skull (Håkansson *et al.*, 1986). The skin between the device and the skull acts as a spring and ultimately dominates the measured signal (Stenfelt & Goode, 2005b).

2.1.4 *Resonant Frequencies*

It is generally accepted that the skull behaves as a rigid body at low frequencies (Håkansson *et al.*, 1986, 1994) with resonances occurring at higher frequencies, however the exact frequency of the first resonance varies widely within the literature. Kirikae (1959) found the first skull resonance to occur between 1700 and 1800 Hz for three dry human skulls, a skull filled with water or jelly, and a cadaver head. The values reported from this study are significantly higher than others reported in the literature and this invariability across different experimental conditions is also not supported. For instance, Franke (1956) found the first resonant frequency of a dry human skull and a cadaver head to be 820 Hz and 600 Hz, respectively. When the dry skull was filled with gelatin to better simulate the damping effects of the brain and cerebrospinal fluid, the first resonance was reduced to approximately 500 Hz. The first resonance reported by Stenfelt *et al.* (2000) for a dry human skull equipped with viscous damping material to better simulate a real human head was 1200 Hz. Khalil *et al.* (1979) obtained the resonant frequencies of two dry human skulls, one male and one female, up to 5000 Hz. They reported a total of 11 resonant frequencies for the male skull with the first occurring at 1385 Hz and six resonant frequencies for the female skull with the first occurring at 1641 Hz. Håkansson *et al.* (1986) obtained an average first resonance of 1000 Hz with a standard deviation of 200 Hz from the mechanical impedance measurements of seven patients with skin penetrating titanium abutments embedded into the skull bone. A later study conducted by Håkansson *et al.* (1994) on six patients with bilateral titanium abutments, found 14–19 resonant frequencies within the frequency range 500–7500 Hz. The average first resonance was at 971 Hz with a standard deviation of 119 Hz. The significant variation in reported values along with the relatively large standard deviations found in the latter two studies suggest the resonant frequencies of the human skull vary widely from subject to subject and may depend on a number of factors including skull size, thickness, and mechanical properties (Håkansson *et al.*, 1986).

2.1.5 *Lateralization*

Sound lateralization occurs when the response of one cochlea is of greater magnitude or ahead in phase of the other. This effect is independent of the location of the stimulation

point, in other words, the response of the contralateral cochlea (opposite side of stimulus) may be of greater magnitude than that of the ipsilateral (same side as stimulus) cochlea as seen in the study conducted by Stenfelt *et al.* (2000). They observed similar levels and phases for frequencies below the first free resonance of the skull (1200 Hz in this study) for both the ipsilateral and contralateral cochleae responses, indicating rigid body behaviour. However, at approximately 800 Hz they noted a large antiresonance in the ipsilateral response, which was not observed in the contralateral response. This effect was also psychoacoustically confirmed in this study, indicating a lateralization effect towards the contralateral side at 800 Hz (Stenfelt *et al.*, 2000). Similar findings to this work were reported by Eeg-Olofsson *et al.* (2008) in cadaver heads where the same antiresonance was observed in the ipsilateral response below the first resonance. This was the only resonance or antiresonance that remained visible and was not smoothed out after the results were averaged across all seven of the cadaver heads measured (Eeg-Olofsson *et al.*, 2008).

2.1.6 *Transcranial Attenuation*

Stenfelt *et al.* (2000) found at frequencies above the first resonance, the level of the contralateral response is lower with a pronounced time delay when compared with the ipsilateral response indicating more complex, non-rigid body motion to be taking place. Similarly, Stenfelt & Goode (2005b) found that the greatest difference in responses in terms of level and phase between the two cochleae was observed when the excitation site was nearest to the cochlea. The ipsilateral response level became greater with less time delay as the stimulation site neared the cochlea (Stenfelt & Goode, 2005b). This result is consistent with Eeg-Olofsson *et al.* (2008) findings that showed an increase in the velocity of the cochlea for positions closer to the cochlea than the conventional location of a Baha[®], with the greatest response observed when excitation was in the proximity of the otic capsule. Stenfelt & Goode (2005b) concluded that the lowest response level was generated when the stimulation position was on the mid-sagittal plane of the skull.

Given their findings, Eeg-Olofsson *et al.* (2008) suggest that bone conduction transmission is most efficient when the stimulation site is on the mastoid surface that attaches to the petrous part of the temporal bone than if it was outside this area. Eeg-Olofsson *et al.* (2008) also investigated the effects of the squamosal suture on sound transmission via bone

conduction, however no conclusive findings on whether this suture is detrimental or not were found.

2.1.7 *Wave Propagation in Skull Bone*

The dispersion relationship, which indicates how frequency changes with wave number, can be used to determine the type of wave propagating through the skull bone. From the dispersion relationship, two wave velocities can be calculated; the phase velocity, v_p and the group velocity, v_g , which are given by:

$$v_p = \frac{f}{k} \quad (2.1a)$$

$$v_g = \frac{\partial f}{\partial k} \quad (2.1b)$$

where f is the frequency and k is the wave number. The phase velocity is the velocity at which the phase of a single frequency component in the overall wave travels. The group velocity is the velocity at which the envelope of the wave, or overall shape of the wave's magnitudes, travels. Non-dispersive behaviour is characterized by a linear dispersion relationship, where the phase and group velocities are equivalent and constant over all frequencies. For dispersive behaviour the dispersion relationship is non-linear, and the phase and group velocities are frequency dependent.

There have been many investigations of wave propagation in the human skull albeit with differing results and conclusions. Tonndorf (1966) initially proposed that waves propagate through the cranial bone as bending or flexural waves in plates. This type of wave is dispersive, and both the phase and group velocity must depend on the square-root of frequency (see Section 2.2 for further details). Zwislocki (1953) investigated this hypothesis up to 2600 Hz but found the phase velocity to be independent of frequency with a constant value of 260 m/s. Franke (1956) also studied this theory and found evidence of dispersion, however not the square root dependence indicative of flexural waves. Instead, the group velocity was found to be approximately linear with respect to frequency between 500 and 1000 Hz. Below and above this region, up to 1600 Hz, the group velocity was constant.

With no indication of flexural waves found in these studies, Tonndorf & Jahn (1981) revised

the initial hypothesis to “plate” waves, which are characterized by a frequency-independent phase velocity. Tonndorf & Jahn (1981) conducted a similar experiment to Zwislocki (1953) with comparable results, finding a constant phase velocity of 330 m/s up to 4000 Hz.

A more recent study by Stenfelt & Goode (2005b) found the phase velocity to depend on frequency in the cranial bone, however less dispersion was observed at frequencies about 2000 Hz. With excitation closer to the cochlea, where the waves were thought to transmit primarily through the skull base, phase velocity was near constant above 2000 Hz (Stenfelt & Goode, 2005b). It was suggested that wave propagation in the thicker bone of the base of the skull is primarily in the form of longitudinal waves, while in the cranial bone more complex waves may exist, including flexural waves.

The term “plate” waves used by some in the literature refers to extensional waves in plates. Extensional and flexural waves are the two types of Lamb waves that can exist in solid plates. Further explanation of Lamb waves can be found in Section 2.2. The skull can only be modeled as a plate at the high frequencies of human hearing, where the wavelength is much smaller than the radius of curvature resulting in relatively uniform material and geometric properties over one wavelength.

If, instead, a human skull can be modeled as a spherical shell, then perhaps this model can be applicable over the entire hearing range. Von Békésy compared the modes of vibration of the human skull to those of a spherical shell and found them to be similar (source: Stenfelt & Goode (2005a)). At 200 Hz the skull behaves as a rigid body. At 800 Hz the forehead and occiput vibrate with opposite phase with a nodal line between them. At 16000 Hz the skull is separated into four quadrants by nodal lines. The top and bottom of the skull vibrate with opposite phases as do the two temporal bones. Kirikae (1959) observed similar modes of vibration. Franke (1956) also considered a closed spherical shell to be a suitable model for vibrations in a skull after comparing their mode shapes, specifically the nodal lines.

It is evident that there are conflicting findings in the literature surrounding wave propagation in the skull. Some researchers have found evidence of extensional plate waves, while others have found spherical shell models better represent the wave behaviour in the

skull. Understanding how waves propagate in the skull is fundamental in gaining a better appreciation for the mechanisms of bone conducted sound. This proves to be an active area of research that warrants further study.

2.2 Lamb Waves

Sir Horace Lamb was one of the first to study waves in an infinite uniform plate (Lamb, 1917). The following section will derive the Lamb frequency equations for a thin isotropic plate of thickness $2h$. The reader is referred to the work of Amirkulova (2011) for a thorough derivation.

A coordinate system is defined with the x and z axes lying on the midsurface of the plate and the y axis perpendicular to this plane. Figure 2.1 show this coordinate system with the z axis pointing out of the page.

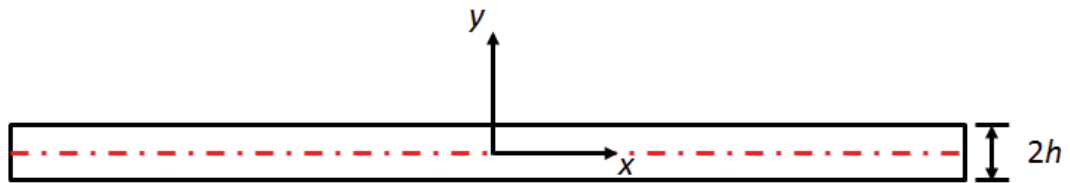


Figure 2.1: Plate of thickness $2h$ in plane strain. The z axis points out of the page.

Assuming plane strain, particle motion is limited to the x and y directions only, therefore the displacement components u and v are

$$u = u(x, y, t) \quad (2.2a)$$

$$v = v(x, y, t) \quad (2.2b)$$

where t is time. Neglecting body forces, the equations of motion are

$$\frac{\partial \sigma_{xx}}{\partial x} + \frac{\partial \sigma_{xy}}{\partial y} = \rho \frac{\partial^2 u}{\partial t^2} \quad (2.3a)$$

$$\frac{\partial \sigma_{xy}}{\partial x} + \frac{\partial \sigma_{yy}}{\partial y} = \rho \frac{\partial^2 v}{\partial t^2} \quad (2.3b)$$

where σ_{ij} are the stress tensors and ρ is the density of the plate. Hooke's law equations are

$$\sigma_{xx} = \lambda_l \left(\frac{\partial u}{\partial x} + \frac{\partial v}{\partial y} \right) + 2\mu_l \frac{\partial u}{\partial x} \quad (2.4a)$$

$$\sigma_{yy} = \lambda_l \left(\frac{\partial u}{\partial x} + \frac{\partial v}{\partial y} \right) + 2\mu_l \frac{\partial v}{\partial y} \quad (2.4b)$$

$$\sigma_{xy} = \mu_l \left(\frac{\partial u}{\partial y} + \frac{\partial v}{\partial x} \right) \quad (2.4c)$$

where μ_l and λ_l are the Lamé elastic coefficients that are related to the material properties of the plate by:

$$\mu_l = G = \frac{E}{2(1 + \nu)} \quad (2.5a)$$

$$\lambda_l = \frac{2G\nu}{1 - 2\nu} \quad (2.5b)$$

where E is the Young's modulus, G is the shear modulus, and ν is the Poisson's ratio. Substituting (2.5) into (2.4) and then substituting into (2.3) gives

$$\frac{\partial^2 u}{\partial x^2} + \frac{1}{1 - \nu} \frac{\partial^2 v}{\partial x \partial y} + \frac{1 - 2\nu}{2(1 - \nu)} \frac{\partial^2 u}{\partial y^2} = \frac{1}{c_1^2} \frac{\partial^2 u}{\partial t^2} \quad (2.6a)$$

$$\frac{\partial^2 v}{\partial y^2} + \frac{1}{1 - \nu} \frac{\partial^2 u}{\partial x \partial y} + \frac{1 - 2\nu}{2(1 - \nu)} \frac{\partial^2 v}{\partial x^2} = \frac{1}{c_2^2} \frac{\partial^2 v}{\partial t^2} \quad (2.6b)$$

where c_1 and c_2 are the longitudinal and transverse wave velocities, respectively, and can be written in terms of the Lamé elastic coefficients and density:

$$c_1^2 = \frac{\lambda_l + 2\mu_l}{\rho} \quad (2.7a)$$

$$c_2^2 = \frac{\mu_l}{\rho} \quad (2.7b)$$

$$(2.7c)$$

and

$$\kappa^2 = \frac{c_1^2}{c_2^2} = \frac{\lambda_l + 2\mu_l}{\mu_l} \quad (2.7d)$$

Since particle motion is limited to the xy plane, the Helmholtz displacement decomposition is simplified to

$$u = \frac{\partial \varphi}{\partial x} + \frac{\partial \psi_z}{\partial y} \quad (2.8a)$$

$$v = \frac{\partial \varphi}{\partial y} - \frac{\partial \psi_z}{\partial x} \quad (2.8b)$$

where φ is a scalar potential function and ψ_z is a vector potential function, which satisfy the 2D wave equations:

$$\frac{\partial^2 \varphi}{\partial x^2} + \frac{\partial^2 \varphi}{\partial y^2} = \frac{1}{c_1^2} \frac{\partial^2 \varphi}{\partial t^2} \quad (2.9a)$$

$$\frac{\partial^2 \psi_z}{\partial x^2} + \frac{\partial^2 \psi_z}{\partial y^2} = \frac{1}{c_2^2} \frac{\partial^2 \psi_z}{\partial t^2} \quad (2.9b)$$

Assuming traveling waves in the x direction and standing waves in the y gives the solutions to (2.9) in the form

$$\varphi = \Phi(y)e^{i(kx-\omega t)} \quad (2.10a)$$

$$\psi_z = i\Psi(y)e^{i(kx-\omega t)} \quad (2.10b)$$

where ω is the angular frequency. Substituting (2.10) into (2.8) gives

$$u = i \left(k\Phi + \frac{d\Psi}{dy} \right) e^{i(kx-\omega t)} \quad (2.11a)$$

$$v = \left(\frac{d\Phi}{dy} - ik\Psi \right) e^{i(kx-\omega t)} \quad (2.11b)$$

and subsequent substitution into (2.9) gives the Helmholtz equations

$$\frac{d^2 \Phi}{dy^2} + \alpha^2 \Phi = 0 \quad (2.12a)$$

$$\frac{d^2 \Psi}{dy^2} + \beta^2 \Psi = 0 \quad (2.12b)$$

where α and β are the longitudinal and transverse wave numbers, respectively, given by

$$\alpha^2 = \frac{\omega^2}{c_1^2 - k^2} \quad (2.13a)$$

$$\beta^2 = \frac{\omega^2}{c_2^2 - k^2} \quad (2.13b)$$

The solutions to (2.12) are

$$\Phi(y) = A \sin \alpha y + B \cos \alpha y \quad (2.14a)$$

$$\Psi(y) = C \sin \beta y + D \cos \beta y \quad (2.14b)$$

Substituting (2.14) into (2.10) and (2.11) gives the following potentials and displacement equations:

$$\varphi = (A \sin \alpha y + B \cos \alpha y) e^{i(kx - \omega t)} \quad (2.15a)$$

$$\psi_z = (C \sin \beta y + D \cos \beta y) e^{i(kx - \omega t)} \quad (2.15b)$$

$$u = i [k(A \sin \alpha y + B \cos \alpha y) + \beta(C \sin \beta y - D \cos \beta y)] e^{i(kx - \omega t)} \quad (2.15c)$$

$$v = [\alpha(A \sin \alpha y - B \cos \alpha y) - ik(C \sin \beta y + D \cos \beta y)] e^{i(kx - \omega t)} \quad (2.15d)$$

Rewriting (2.4) in terms of the potentials φ and ψ_z , and substituting in (2.15) gives following expressions for the stresses:

$$\sigma_{xx} = \mu_l \left[[2\alpha^2 - \kappa^2(k^2 + \alpha^2)] (A \sin \alpha y + B \cos \alpha y) - 2k\beta(C \cos \beta y - D \sin \beta y) \right] e^{i(kx - \omega t)} \quad (2.16a)$$

$$\sigma_{yy} = \mu_l \left[[2k^2 - \kappa^2(k^2 + \alpha^2)] (A \sin \alpha y + B \cos \alpha y) + 2k\beta(C \cos \beta y - D \sin \beta y) \right] e^{i(kx - \omega t)} \quad (2.16b)$$

$$\sigma_{xy} = i\mu_l \left[2\alpha k(A \cos \alpha y - B \sin \alpha y) - 2(\beta^2 - k^2) (C \sin \beta y + D \cos \beta y) \right] e^{i(kx - \omega t)} \quad (2.16c)$$

The $e^{i(kx - \omega t)}$ term is omitted for the remainder of this derivation as it does not affect the frequency equation. Using symmetry in the yz plane, u and v are symmetric about $y = 0$ if they contain cosines and sines, respectively, and conversely, u and v are antisymmetric about $y = 0$ if they contain sines and cosines, respectively. Thus, by inspection of (2.16) it

is apparent that the wave motion can be separated into symmetric modes of vibration:

$$\sigma_{xx} = \mu_l \left[[2\alpha^2 - \kappa^2(k^2 + \alpha^2)] B \cos \alpha y - 2k\beta C \cos \beta y \right] \quad (2.17a)$$

$$\sigma_{yy} = \mu_l \left[[2k^2 - \kappa^2(k^2 + \alpha^2)] B \cos \alpha y + 2k\beta C \cos \beta y \right] \quad (2.17b)$$

$$\sigma_{xy} = -i\mu_l \left[2\alpha k B \sin \alpha y + (\beta^2 - k^2) C \sin \beta y \right] \quad (2.17c)$$

and antisymmetric modes of vibration:

$$\sigma_{xx} = \mu_l \left[[2\alpha^2 - \kappa^2(k^2 + \alpha^2)] A \sin \alpha y + 2k\beta D \sin \beta y \right] \quad (2.18a)$$

$$\sigma_{yy} = \mu_l \left[[2k^2 - \kappa^2(k^2 + \alpha^2)] A \sin \alpha y - 2k\beta D \sin \beta y \right] \quad (2.18b)$$

$$\sigma_{xy} = i\mu_l \left[2\alpha k A \cos \alpha y - 2(\beta^2 - k^2) D \cos \beta y \right] \quad (2.18c)$$

with respect to the $y = 0$ plane resulting in two infinite sets of modes. Assuming traction free boundaries, the boundary conditions are

$$\sigma_{yy} = \sigma_{xy} = \sigma_{zy} = 0, \quad \text{at } y = \pm h \quad (2.19)$$

Substituting (2.17b) and (2.17c) into (2.19) gives a homogeneous system of equations in terms of the coefficients B and C :

$$(k^2 - \beta^2)B \cos \alpha h + 2\beta k C \cos \beta h = 0 \quad (2.20a)$$

$$\mp [2k\alpha B \sin \alpha h + (k^2 - \beta^2)C \sin \beta h] = 0 \quad (2.20b)$$

Taking the determinant of (2.20) gives the Lamb frequency equation for the symmetric mode:

$$\frac{\tan \beta h}{\tan \alpha h} = -\frac{4k^2\alpha\beta}{(k^2 - \beta^2)^2} \quad (2.21)$$

Similarly, substituting (2.18a) and (2.18c) into (2.19) gives a homogeneous system of equations in terms of the coefficients A and D :

$$\pm [(k^2 - \beta^2)A \sin \alpha h - 2\beta k D \sin \beta h] = 0 \quad (2.22a)$$

$$2k\alpha A \cos \alpha h - (k^2 - \beta^2)D \cos \beta h = 0 \quad (2.22b)$$

Taking the determinant of (2.22) gives the Lamb frequency equation for the antisymmetric

mode:

$$\frac{\tan \beta h}{\tan \alpha h} = -\frac{(k^2 - \beta^2)^2}{4k^2\alpha\beta} \quad (2.23)$$

Solving (2.21) and (2.23) to obtain a relationship between frequency and wave number over all frequencies is not possible analytically, however numerical solutions have been obtained in the literature (Amirkulova, 2011) but are omitted here for brevity. Of interest here are the two zero-order modes of vibration that occur at low frequencies where the wavelength is much larger than the thickness of the plate. These fundamental modes are the only modes that are present over the full frequency spectrum. Figure 2.2 illustrates the symmetric and antisymmetric Lamb wave modes. The symmetric mode is called the extensional mode as the majority of particle motion, indicated by blue arrows in Figure 2.2a, occurs in the x-direction, i.e. direction of wave propagation. By contrast, the antisymmetric mode is referred to as the bending or flexural mode since the particle motion, indicated by blue arrows in Figure 2.2b, is predominately in the direction perpendicular to the plane of the plate. For both types of Lamb waves, the individual particles travel in an elliptical orbit.

In the large wavelength (or low frequency) limit where the zero-order modes exist the relationship between phase velocity and frequency can be obtained from the Lamb frequency equations by taking kh , αh , and βh to be small and applying a Taylor series expansion to (2.21). For the symmetric mode, this expansion is limited to the first order terms

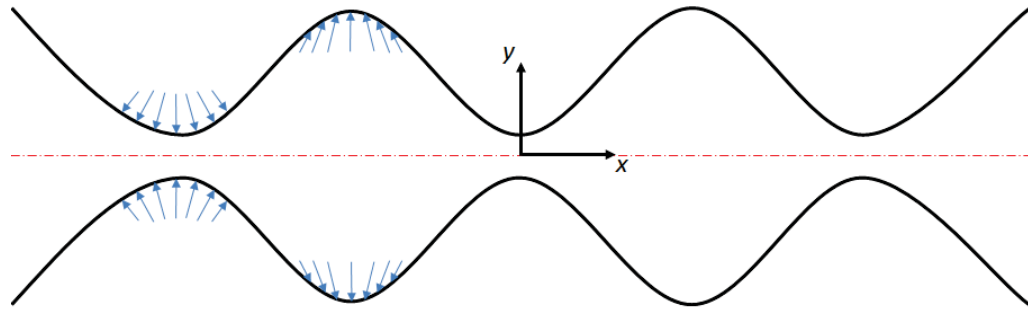
$$\tan \alpha h = \alpha h \quad (2.24a)$$

$$\tan \beta h = \beta h \quad (2.24b)$$

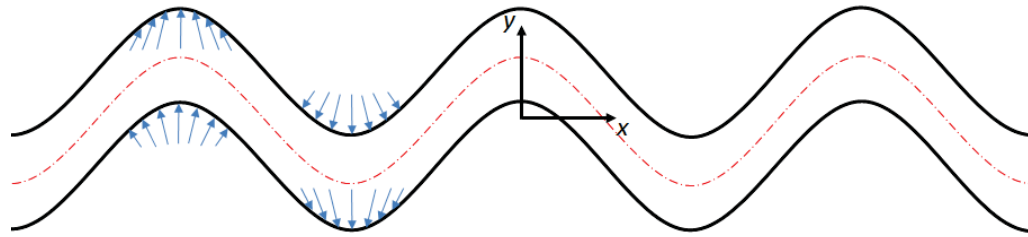
and (2.21) becomes

$$(k^2 - \beta^2)^2 = -4k^2\alpha^2 \quad (2.25)$$

Substituting (2.7d) and (2.13) into (2.25) and rearranging gives the phase velocity of the



(a) Symmetric Mode



(b) Antisymmetric Mode

Figure 2.2: The two zero-order Lamb wave modes of vibration. Vibrations in the y direction are (a) symmetric and (b) antisymmetric about the $y = 0$ plane. The blue arrows represent the local particle motion.

symmetric zero-order mode $v_{p,s}$:

$$v_{p,s}^2 = \frac{\omega^2}{k^2} = 4c_2^2 \left(1 - \frac{1}{\kappa^2} \right)$$

$$v_{p,s} = 2\sqrt{\frac{\mu_l}{\rho} \left(\frac{\lambda_l + \mu_l}{\lambda_l + 2\mu_l} \right)} \quad (2.26)$$

For the antisymmetric mode (2.23) must be expanded to the second order terms in the Taylor series in order to retain the α term in the solution. Therefore,

$$\tan \alpha h = \alpha h \left(1 - \frac{1}{3} \alpha^2 h^2 \right) \quad (2.27a)$$

$$\tan \beta h = \beta h \left(1 - \frac{1}{3} \beta^2 h^2 \right) \quad (2.27b)$$

and (2.23) becomes

$$4k^2\beta^2 \left(1 + \frac{\beta^2 h^2}{3}\right) = -(k^2 - \beta^2)^2 \left(1 + \frac{\alpha^2 h^2}{3}\right) \quad (2.28)$$

Substituting (2.13) into (2.28) and simplifying gives

$$\begin{aligned} 3k^2 h^2 \left(\frac{\omega^2}{k^2 c_2^2}\right)^2 - 4k^2 h^2 \left(\frac{\omega^2}{k^2 c_2^2}\right) &= -k^2 h^2 \left(\frac{\omega^2}{k^2 c_1^2}\right) \left(\frac{\omega^2}{k^2 c_2^2}\right)^2 + \\ 4k^2 h^2 \left(\frac{\omega^2}{k^2 c_1^2}\right) \left(\frac{\omega^2}{k^2 c_2^2}\right) - 4k^2 h^2 \left(\frac{\omega^2}{k^2 c_1^2}\right) - 3 \left(\frac{\omega^2}{k^2 c_2^2}\right) & \end{aligned} \quad (2.29)$$

It is reasonable to assume that the terms $\omega^2/k^2 c_1^2$ and $\omega^2/k^2 c_2^2$ are small (Lamb, 1917). Thus, simplifying (2.2) and substituting in (2.7d) results in the phase velocity of the antisymmetric zero-order mode $v_{p,a}$:

$$\begin{aligned} v_{p,a}^2 &= \frac{\omega^2}{k^2} = \frac{4}{3} k^2 h^2 \left(1 - \frac{1}{\kappa^2}\right) \\ v_{p,a} &= 2kh \sqrt{\frac{1}{3} \frac{\mu_l}{\rho} \left(\frac{\lambda_l + \mu_l}{\lambda_l + 2\mu_l}\right)} \end{aligned} \quad (2.30)$$

The symmetric mode is non-dispersive in the zero-order limit since (2.26) does not depend on frequency. Conversely, the antisymmetric mode is dispersive in the zero-order limit since (2.30) depends on the wave number and, subsequently, the frequency. Specifically, the phase velocity is linearly dependent on the wave number or, equivalently, dependent on the square root of frequency.

2.3 Spherical Shells

Many solutions to the vibration problem of spherical shells exist in the literature but with minor variations that are primarily due to differences in the strain-displacement relationships used (Junger & Feit, 1972). The comparison of the strain energy due to stretching and bending of the shell is used to distinguish between the two infinite sets of modes that exist in the frequency spectrum; membrane modes and bending or flexural modes (Kalnins, 1964). The upper branch consisting of the membrane modes can be

obtained by using either membrane or bending theories, however the lower branch of bending modes cannot be accurately predicted by the membrane theory (Kalnins, 1964). Membrane theory does not account for bending, which causes the lower branch solution to approach a frequency limit thereby causing the intervals between natural frequencies to approach zero (Baker, 1961).

The following section will consider the solution presented by Junger & Feit (1972) to the free axisymmetric non-torsional vibrations of a closed, thin spherical shell with mean radius r and thickness h . A linear formulation is assumed since the deformations are small with respect to the thickness of the shell, and, in turn, the thickness of the shell is small with respect to the radius of curvature of the shell. The Kirchhoff-Love theory assumption reduces the formulation to deformations of the shell's midsurface only. The solution employs the Hamilton's variational principle, which uses kinetic and strain energies to obtain the spherical shell equations of motion. Bending stresses are taken into account in the strain energy term. From the equations of motion the following frequency equation for free axisymmetric vibrations of a spherical shell is obtained:

$$\begin{aligned} \Omega^4 - [1 + 3\nu + \lambda_n - \beta^2(1 - \nu - \lambda_n^2 - \nu\lambda_n)]\Omega^2 + (\lambda_n - 2)(1 - \nu^2) \\ + \beta^2[\lambda_n^3 - 4\lambda_n^2 + \lambda_n(5 - \nu^2) - 2(1 - \nu^2)] = 0 \end{aligned} \quad (2.31)$$

where ν is the Poisson's ratio, $\beta^2 = \frac{h^2}{12r^2}$, and $\lambda_n = n(n+1)$, where n is the mode number. The dimensionless frequency Ω is given by:

$$\Omega = \frac{\omega r}{v_p} \quad (2.32)$$

where ω is the angular frequency and the phase velocity of compressional waves in an elastic plate v_p is given by:

$$v_p = \sqrt{\frac{E}{\rho(1 - \nu^2)}} \quad (2.33)$$

where E is the Young's modulus and ρ is the volumetric density of the shell. This solution is consistent with other formulations in the literature that employ bending theory in order to accurately predict the bending modes (Kalnins, 1964; McIvor & Sonstegard, 1966; Engin & Liu, 1970).

Using the quadratic equation to solve for the roots of (2.31) in terms of Ω yields two frequency equations; the membrane solution and the flexural solution. Figure 2.3 plots the two branches using parameters consistent with human cranial bone listed in Table 2.1.

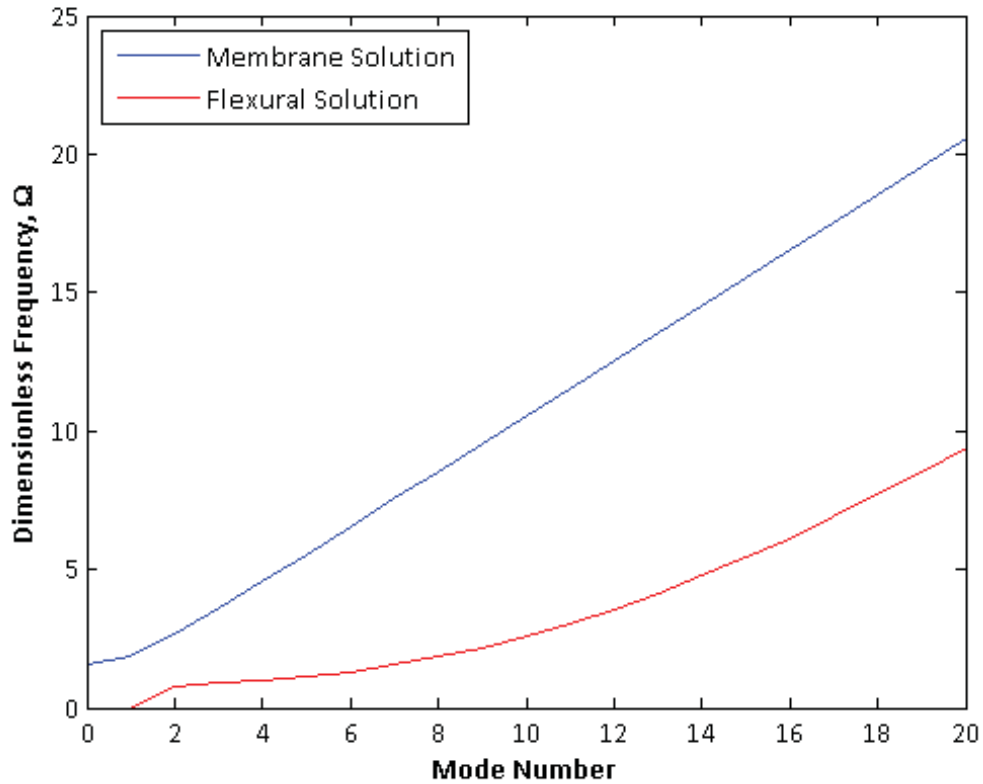


Figure 2.3: Spherical shell model with average skull parameters given in Table 2.1

Table 2.1: Average skull parameters used to generate Figure 2.3

Parameter	Symbol	Value	Reference
Young's modulus	E	5.5 GPa	(McElhaney <i>et al.</i> , 1970)
Poisson's ratio	ν	0.2	(McElhaney <i>et al.</i> , 1970)
density	ρ	1400 kg/m ³	(McElhaney <i>et al.</i> , 1970)
thickness	h	7 mm	(McElhaney <i>et al.</i> , 1970)
radius	r	90 m	Back calculated from circumference of young adult (Eichorn & Bayley, 1962)

2.4 Measurement Techniques

A number of measurement techniques have been used to study the vibratory response of human skulls and cadaver heads. Generally, these techniques can be separated into contact and non-contact measurement devices.

2.4.1 *Contact Measurement Devices*

Contact measurement devices, such as accelerometers and impedance heads, have been used extensively to measure various vibratory characteristics of human skulls and cadaver heads (Håkansson *et al.*, 1986, 1996; Stenfelt *et al.*, 2000). Contact devices are rigidly fixed to the measurement object and collect discrete point measurements. They are capable of acquiring 3D data but are a physical mass that must be moved from site to site across the head. This is additional mass to the system must be accounted for when interpreting the results. Attaching contact devices may be problematic if the measurement object is small or hot, or if the surface to be measured is difficult to access.

2.4.2 *Non-Contact Measurement Devices*

Non-contact measurements include holography and laser Doppler vibrometry. The major benefit to these techniques over contact devices is there is no mass-loading of the system. Holography acquires a time averaged hologram of the vibrating surface and has been used by Hoyer & Dörheide (1983) to study the response of cadaver heads. Laser Doppler vibrometers (LDVs) have become an increasingly popular vibration measurement device, especially when the surface is small and difficult to reach. A number of researchers have used laser Doppler vibrometry to study the vibratory response of the stapes (Huber *et al.*, 2008; Sim *et al.*, 2010), cochlea (Eeg-Olofsson *et al.*, 2008) and human skull (Trnka *et al.*, 2004). The following section will give an in depth overview of laser Doppler vibrometry.

2.4.3 *Laser Doppler Vibrometry*

Laser Doppler vibrometry is a non-contact measurement technique used to measure the vibratory response of a surface. There are several different types of laser Doppler vibrometers (LDVs), including single-point, scanning and 3D LDVs. Figure 2.4 shows a schematic of the general principle behind a LDV.

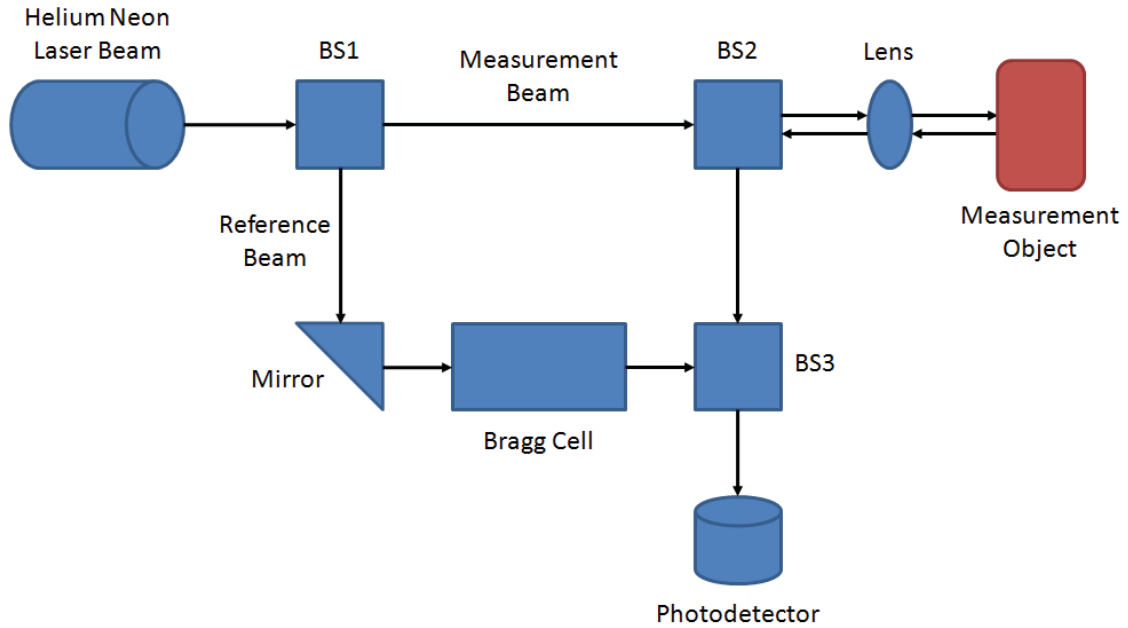


Figure 2.4: Schematic of a laser Doppler vibrometer (LDV) (Adapted from Polytec GmbH (2012))

A helium neon laser beam, with a frequency $f = 4.74 \times 10^{14}$ Hz and a wavelength $\lambda = 633$ nm), is split by a beam splitter (BS1) into two separate beams, a measurement beam and a reference beam. The measurement beam passes through a second beam splitter (BS2) and is focused by a lens to a point on the surface of the measurement object. Movement of the object parallel to the laser beam will cause a shift in the frequency of the incident beam. This shift is called the Doppler frequency shift f_d and is proportional to the velocity of the object by:

$$f_d \propto \frac{2v_s}{\lambda} \quad (2.34)$$

where v_s is the surface velocity and λ is the wavelength of the laser beam. The backscattered light from the measurement object is then deflected by BS2 to a third beam splitter (BS3), where it is combined with the reference beam. This merged beam is then directed to the photodetector, where an interference pattern is generated. The LDV can obtain the displacement data by counting the dark-bright fringes on the detector. One complete dark-bright cycle corresponds to the measurement surface displacing exactly half the wavelength of the incident helium neon laser beam (316 nm). By applying interpolation techniques a displacement resolution of 2 nm can be obtained (Polytec GmbH, 2012).

The LDV can also obtain velocity data from the interference pattern. The difference in frequency between the reference and measurement beams appears as an intensity modulation in the interference signal. By demodulating this signal, the Doppler frequency shift and, subsequently, the velocity of the object can be determined.

The interference pattern for a surface moving towards the laser head will be the same as that for a surface moving away from the laser head. In order to distinguish between these two interference patterns, a heterodyne interferometer regime is employed by introducing an acousto-optic modulator, or Bragg cell, that statically shifts the frequency of the reference beam by $f_b = 40$ MHz (Polytec GmbH, 2012). The initial frequency of the laser beam is significantly higher than f_b and cannot be measured by the photodetector. However, the beat frequency $f_b + f_d$ generated by combining the reference and measurement beams is detectable. Thus, the modulation frequency of the fringe pattern is 40 MHz when the object is stationary, less than 40 MHz when the object is moving towards the interferometer, and greater than 40 MHz when the object is moving away, thereby allowing the direction of vibration to be detected.

As discussed above, an LDV can either use displacement demodulation, where the dark-bright fringes of the interference pattern are counted, or velocity demodulation, where the Doppler shift is given as a voltage that is proportional to the velocity of the vibrating surface (Polytec GmbH, 2012). At low frequencies, the amplitudes of vibration are larger, and thus displacement demodulation is preferred. At high frequencies, the vibrations have significantly smaller amplitudes but larger velocities, and thus velocity demodulation is preferred.

The following subsections discuss two types of three-dimensional (3D) LDVs manufactured by Polytec (Waldbronne, DE) that were used to conduct two different experiments on dry human skulls. These experiments are discussed in detail in Chapter 3.

2.4.3.1 Single-Point 3D LDV

The single-point 3D LDV consists of three separate laser beams originating from one laser head that is mounted on a tripod. The three laser beams, whose axes are oriented in three non-collinear directions, are manually focused to a single point on the measurement surface as shown in Figure 2.5.



Figure 2.5: Polytec's 3D single point laser Doppler vibrometer (LDV) mounted on a tripod.

The velocity is measured parallel to each of the three laser beam axes, giving the 3D vibratory response of the measurement surface at a given point. Since the laser beams are housed in one laser head, the focal length is relatively short, thereby giving a comparably higher signal-to-noise ratio (SNR) to the system.

2.4.3.2 Scanning 3D LDV

The scanning 3D LDV consists of three laser heads each containing a single laser beam as shown in Figure 2.6. The laser heads are mounted on a custom tripod and oriented in a triangular formation with an 85 cm separation between adjacent laser heads. The tripod is seated on an isolated vibration platform. The three laser beams converge to a single laser spot on the measurement surface by the use of two galvanometric mirrors contained in each laser head. These mirrors also allow the laser spot to be scanned through a virtual grid of scan points that is defined over the video image of the measurement surface. The velocity of the surface is measured parallel to each of the three laser beams resulting in the

3D vibratory response at each scan point.

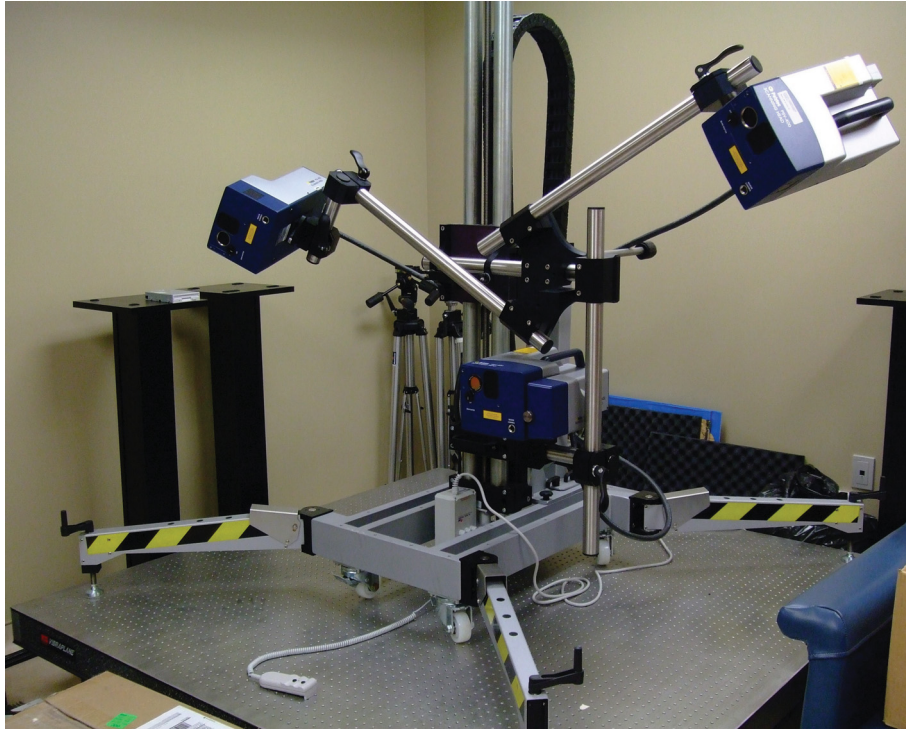


Figure 2.6: Polytec's 3D scanning laser Doppler vibrometer (LDV). The three laser heads are mounted on a custom tripod, which is seated on an isolated vibration platform.

The center laser head (referred to as the Top laser for the remainder of this document) contains a geometry scan unit which measures the distance to each scan point. This is used to determine the coordinates of all the scan points in the grid and effectively captures the geometry of the measurement surface. Only one side of the measurement object can be scanned at one time, however a coordinate system can be defined using the geometry scan unit and, if applied to subsequent scans, allows multiple measurements views to be stitched together in post-processing of the data.

CHAPTER 3

EXPERIMENTATION

Three experiments, Experiment 1, Experiment 2 and Experiment 3, were used to investigate the vibratory response of dry human skulls. Experiment 1 and Experiment 2 tested the same two dry human skulls shown in Figure 3.1 that were purchased from SawBone® (Pacific Research Laboratories, Inc., Vashon, WA). Skull A and Skull B had masses of 440.27 g and 651.78 g, respectively. Skull A's mandible was attached to the rest of the skull by two linear springs. Skull B's mandible was detached from the rest of the skull and was not included in the experimental measurements. Experiment 3 only used Skull B. During

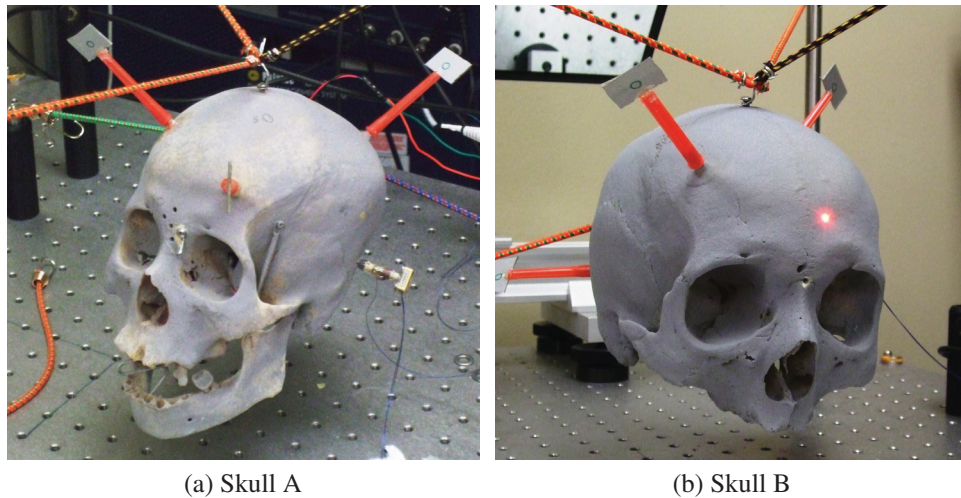


Figure 3.1: The two dry human skulls used in Experiments 1 - 3.

all experiments the skulls were suspended using an elastic suspension system which was rigidly mounted onto an isolated vibration table as shown in Figure 3.2. The resonance

of the suspension system was less than 2 Hz, which was well below the frequency range of interest in both experiments. This section outlines the skull preparation, experimental setup and preliminary data processing for each experiment.

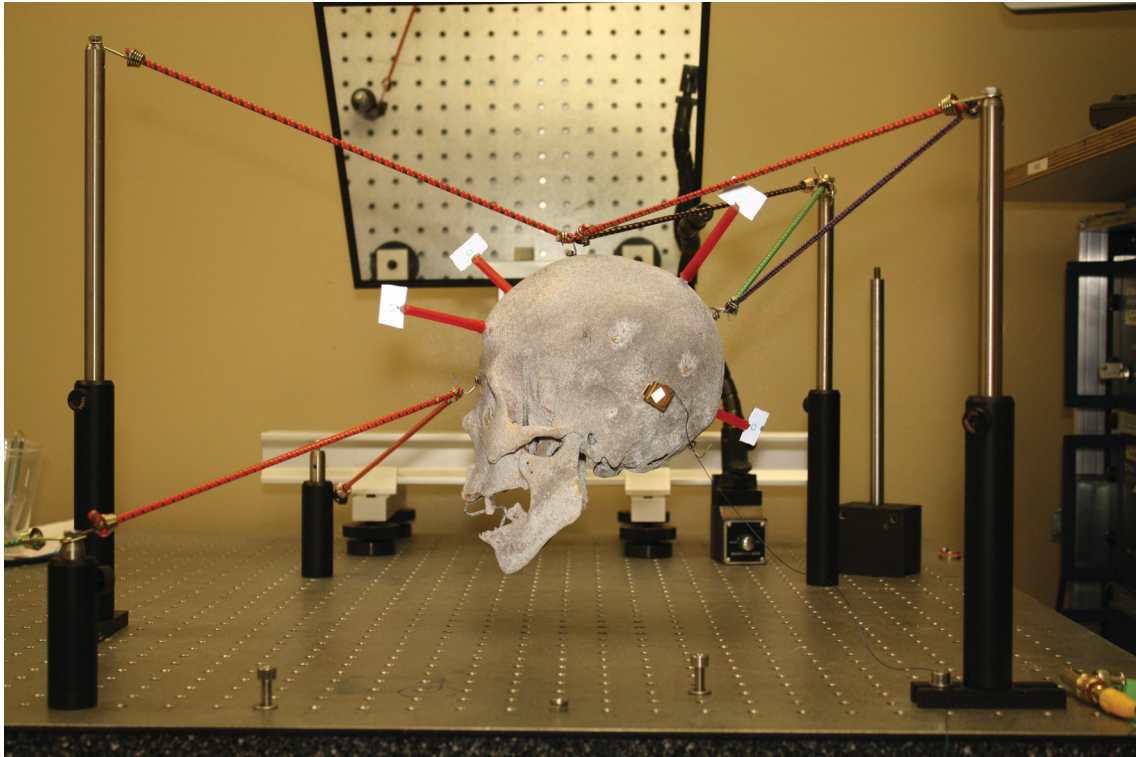


Figure 3.2: Skull A mounted in left-view orientation on the elastic suspension system. The bone vibrator from a Baha® Divino™ (gold and white box) is attached to the left temporal bone via an implanted abutment. All four coordinate system markers are visible.

3.1 Experiment 1

Experiment 1 investigates the vibratory response of a skull over all frequencies within a range by obtaining spectrally high resolution data.

3.1.1 Skull Prep

Four small screws with fitted hooks were drilled into each skull to be used as mounting points for the elastic suspension system. The skulls were coated in one layer of retroreflective spray paint (US Reflector, Worcester, MA) to increase the reflectivity of the surface.

A Baha[®] abutment was implanted in the left temporal bone of each skull via a 4 mm self-tapping screw that once implanted was able to withstand a minimum of 40 N·cm of torque. The recommended surgical location was used; 55 mm from the ear canal centre at 36° from the Frankfurt line (Tjellström *et al.*, 2001), which connects the base of the eye socket to the top of the ear canal. A bone vibrator taken from a Baha[®] Divino[™] hearing aid was then attached to the implanted abutment.

3.1.2 Setup

In order to obtain data over all frequencies within a range a swept sine input was used, which required a relatively high signal to noise ratio (SNR). For this reason, the single-point 3D LDV was used to acquire the vibratory response of the skull due to its relatively short focal length. Polytec Vibrometer Software (VibSoft 4.5) was used to interface with the LDV as per the manufacturer's recommendation. The Baha[®] was excited with a burst chirp signal generated by the PSV software and amplified by an external audio amplifier. The total frequency range, 0.1 - 20 kHz, was tested in three smaller ranges to ensure appropriate settings were being used for each frequency level. Table 3.1 summarizes the software acquisition settings used for each frequency range. The settings were chosen for each frequency range such that the frequency response of the input signal was flat and the coherence signal was as close to unity as possible. The frequency range of interest lies within the start and end frequencies of the burst chirp signal to ensure the desired data was acquired during the cleanest segment of the input signal. Therefore, in each of the three ranges, the data was truncated at the start and end frequencies of interest before being processed.

Table 3.1: Experiment 1: Acquisition settings

Frequency Range (kHz)	Complex Averages	Bandwidth (kHz)	FFT Lines	Burst Chirp Signal		
				Amp. (V)	Start Freq. (Hz)	End Freq. (Hz)
Low: 0.1–5	100	8	12,800	0.1	10	7,000
Mid: 5–10	100	12.5	12,800	0.2	4,000	12,000
High: 10–20	100	25	12,800	0.7	9,000	24,000

Four separate channels were used to acquire data. The vibrometer channel, Vib 3D, recorded the amplified input signal while the three reference channels, Ref1, Ref2 and Ref3, recorded the three non-collinear velocity components, respectively. The generated input signal was used as a trigger to ensure meaningful phase data was acquired and to allow multiple measurements from one site to be averaged together. Table 3.2 gives the software settings used for each acquisition channel. Note that the range of each channel is dependent on the frequency range being measured.

Table 3.2: Experiment 1: Channel settings

Channel	Direction	Quantity	Sensitivity (mm/s/V)	Range (V)		
				Low	Mid	High
Vib 3D	+z	Voltage	1	1	1	3.162
Ref1	+x	Velocity	0.005	1	3.162	3.162
Ref2	+y	Velocity	0.005	1	3.162	3.162
Ref3	+z	Velocity	0.005	1	3.162	3.162

The surface velocity was measured at five discrete locations spaced out over the cranium of a dry human skull prepared as per section 3.1.1. The LDV was manually focused to each measurement point and aligned such that the laser head axis was perpendicular with the skull surface. The complex average of 100 data acquisitions was performed in the time domain by the PSV software for each of the five locations. The multiple experimentation sites and complex averaging further increased the SNR of the system and produced data which better represented the skull as a whole. In order to obtain the admittance data of the system, the input force was required. The motion of the motor creates an equal and opposite reaction force on the skull due to the conservation of momentum. Thus, the force was calculated by measuring the acceleration of the Baha[®] casing parallel to the abutment axis then multiplying this data by the effective mass of the Baha[®]. The range for the software channel settings for the acceleration measurement were changed since the motion of the motor casing was greater than the motion of the skull surface. The ranges for the acceleration measurement are listed in Table 3.3 for each channel at each frequency range, respectively. All other settings remained unchanged from the surface velocity measurements.

Table 3.3: Experiment 1: Channel range settings for acceleration measurement

Channel	Range (V)		
	Low	Mid	High
Vib 3D	1	1	3.162
Ref1	1	3.162	3.162
Ref2	1	3.162	3.162
Ref3	1	3.162	3.162

3.1.3 Preliminary Post-Processing

The measured vibratory response is recorded as a time signal, which is converted into the frequency spectrum by the PSV software (Polytec GmbH, n.d.b). Since all frequencies from 100–20000 Hz were excited in Experiment 1, the frequency response function could be obtained. The frequency response function of a system is a measure of the magnitude and phase of the output with respect to the input as a function of frequency. There are three different frequency response functions calculated by the PSV software; FRF, H1 and H2. Without averaging, FRF is calculated. With averaging, the user can chose between H1 or H2, which are estimators of the system's frequency response function FRF_{sys} . H1 is sensitive to noise in the reference channels while H2 is sensitive to noise in the vibrometer channel. Since there is minimal noise in the input signal (recorded by the Vib 3D channel), the H2 frequency response function was used. The PSV software calculates the H1 and H2 frequency response functions as per the following equations

$$H1_{VR_i} = \frac{CP_{RV}}{AP_{RR_i}} \quad (3.1)$$

$$H2_{VR_i} = \frac{AP_{VV}}{CP_{VR_i}} \quad (3.2)$$

where AP is the auto power spectra and CP is the cross power spectra. The subscripts V , R_1 , R_2 and R_3 refer to the Vib 3D, Ref1, Ref2 and Ref3 channels, respectively. The auto power spectra AP is given by

$$AP_{VV} = S_V^* S_V \quad (3.3)$$

where the $*$ represents the complex conjugate and S is the spectrum calculated by taking the fast Fourier transform (FFT) of the corresponding channel. The cross power spectra CP is given by

$$CP_{VR_i} = S_V^* S_{R_i} \quad (3.4)$$

The magnitude (dB) and phase ($^\circ$) of the H_{2VR_1} , H_{2VR_2} and H_{2VR_3} frequency response functions were exported from the PSV software to ASCII files and used in the MATLAB[®] code in Appendix A to calculate the admittance for each skull. This code is discussed in greater detail in Section 4.2.

3.2 Experiment 2

Experiment 2 examines the 3D spatial response over the entire surface of the skull at discrete frequencies. Since only one side of the skull could be captured during a given scan, six views of data were collected for each frequency measured. The measurement views were labelled top, bottom, right, left, anterior and posterior, from the perspective of the skull and are shown in Figure 3.3 for Skull B.

3.2.1 Skull Prep

The same skulls prepared as per the procedure in section 3.1.1 were used in Experiment 2 with one minor modification. Experiment 2 requires that a 3D global coordinate system be applied to the skull in order to render the six separate views of data in 3D space. Therefore, four spatial markers were attached to the skull using epoxy in such a way that all four markers were visible in a single view and a minimum of three markers were visible in the remaining five views.

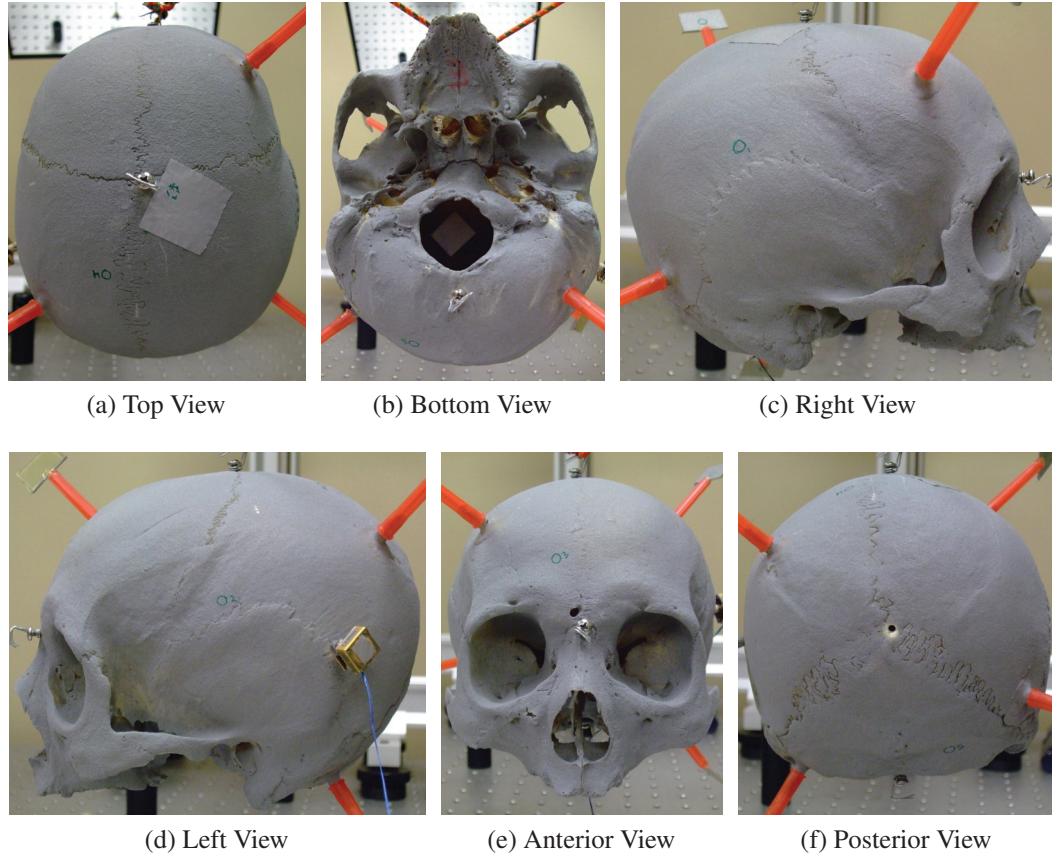


Figure 3.3: The six measurement views used in Experiment 2.

3.2.2 Setup

A scanning 3D LDV was used with PSV 8.6 software (Polytec GmbH, n.d.a) to acquire the three-dimensional vibratory response of the skull. The preliminary setup of this experiment is shown in the wiring diagram in Figure 3.4. The input signal was generated in the software and used as a trigger for data acquisition. This signal was amplified by an external audio amplifier then used to drive the Baha[®]. The signal was recorded by an analog input reference channel, REF21.

The following are the steps used to set up the software and were conducted for all six measurement views. The first view measured was of importance, however, as it was used to define the coordinate system to be used in the remaining five measurement views. This first view required all four spatial markers to be visible in the video image in the software. The following explains the software setup procedure in detail.

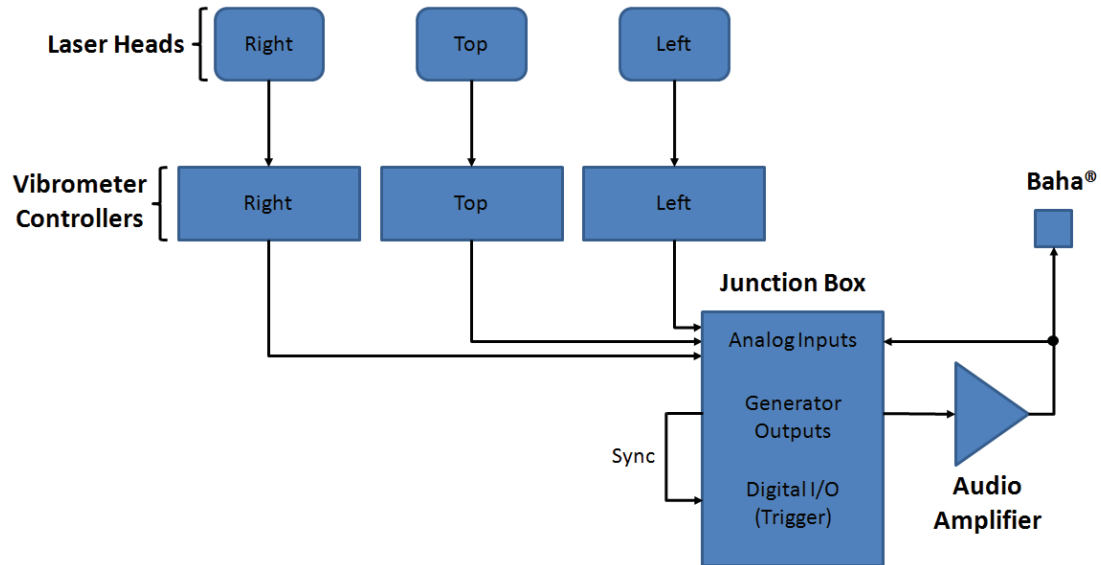


Figure 3.4: Experiment 2: Wiring diagram

All three lasers were turned on before starting the PSV software. The software was then set to "Acquisition Mode" where the live image from the camera could be viewed. The scanning head preferences in the Setup menu had to be updated to ensure the angle of each laser head in the software correctly corresponded with the actual orientation of the laser heads on the custom mounting block shown in Figure 2.6. The head angle of the top, left and right laser heads were set to 0° , 299.5° and 61.5° , respectively. The camera and each of the three lasers were autofocused, upon which each laser's optical signal level meter was reading close to maximum.

Next, a 2D alignment was performed on each laser, which aligns the video image with the position of each laser on the surface to be measured. Each laser requires a minimum of two points with different horizontal and vertical locations for a successful 2D alignment, however the more points used, the more precise the software positions each laser. Therefore, 50–70 alignment points (dependent on size of measurement surface) spread out over the entire skull surface in the given measurement view were found to be adequate. Each alignment point was generated by positioning the laser with the mouse and clicking on the laser spot in the video image. As more alignment points were defined the laser followed the cursor in the software more precisely.

Following the 2D alignment, a 3D coordinate system was defined for the given measurement view via the 3D alignment in the software. Extreme care must be taken in the 3D alignment to ensure the coordinate system is precise and consistent as possible. This will greatly simplify stitching of the measurement views in post-processing of the data, which will be described in detail in Section 3.2.3. The coordinate units were set to mm and the target quality to 1 mm. Firstly, the top laser was aligned separately. This process was different for the first measurement view since this is the step which defines the global coordinate system to be used in the remaining five measurement views. The first view measured required all four spatial markers to be visible in the video image and thereby the top laser beam was able to reach the target on each marker. The "Set New Alignment Point at Laser Spot/Assign Laser Spot to Point" option was selected and the "Auto" box checked. The latter option assigned coordinates to each alignment point automatically via the geometry scan unit located in the middle or top laser head. The "Coordinate Definition Mode" was set to "Origin, Axis, Plane". The top laser was moved to the target on the first spatial marker using the mouse, then the cursor was positioned over the laser spot on the video image, and the left mouse button was clicked to define an alignment point at this location. The right mouse button was clicked on this alignment point and "Origin" was selected. The top laser was then moved to the next spatial marker target, an alignment point defined and assigned "+z-axis". The same procedure was followed for the third spatial marker and assigned "z/+x-plane". For the fourth spatial marker an alignment point was defined but no designation assigned, simply an alignment point. The alignment was calculated. Upon a successful 3D alignment of the top laser, the LED "Status" turned green. If the LED "Status" turned red the alignment of the top laser exceeded the target quality. To improve the alignment quality, new laser positions were assigned to the alignment points that failed and the alignment was recalculated. The coordinates of these four alignment points for the top laser were recorded and used to define the global coordinate system in the remaining five measurement views. Again, diligence must be taken in this step to ensure the coordinate system used is consistent over all measurement views. The top laser alignment for these views was conducted as follows. The "Auto" box was unchecked and the "Assign Coordinates to Point" option was selected. The "Coordinate Definition Mode" was set to "Origin, Axis, Plane". The top laser spot was dragged to the target on the first spatial marker and an alignment point was defined at that location. The coordinate values

for the corresponding spatial marker were then assigned to that alignment point. This was repeated for at least two additional spatial markers. The alignment was then calculated. If the alignment failed, new laser positions were defined for the alignment points that did not meet the target quality and the alignment was recalculated.

The 3D alignment was completed by defining alignment points for the left and right laser heads on the skull surface, using the top laser head to define coordinates to each point with the "Coordinate Definition Mode" set to "Points with Free Coordinates". This process was the same for all six measurement views. For each alignment point the top laser was dragged to the desired location, the cursor was positioned over the laser spot, and the left mouse button was clicked to assign an alignment point to the location. The left laser was then dragged to the same location and the left mouse button was clicked, this time on the existing alignment point. The same procedure was repeated with the right laser head. At least four alignment points, spread out over the measurement surface, were defined. The alignment was then calculated. As with the top laser head alignment, if the LED "Status" turned green for a given laser head, the alignment met the target quality for that laser. However, if the LED "Status" turned red, the alignment failed for that laser and the following adjustments were made. Either new laser positions were assigned to existing alignment points as was done with the top laser alignment, or alignment points were either added or taken away ensuring at least four and no more than seven were present upon recalculation. This was an iterative process and continued until all three laser heads met the target quality. Table 3.4 and Table 3.5 show the top, left and right laser alignment qualities attained for each of the six measurement views for Skull A and Skull B, respectively. All alignment qualities met or exceeded the 1.0 mm target quality and an alignment quality of less than 0.5 mm was achieved for all lasers in all six views for Skull B.

Following the 3D alignment, a grid of scan points was defined. The polygon drawing tool in the "Standard Mode" was used to trace the perimeter of the skull surface in the video image. A hexagonal grid was fit onto the image to fill the measurement surface mapped out by the polygon trace. The density of this grid of trias was set to 40, which produced 550–900 scan points over the surface depending on the measurement view. A geometry scan was then performed using the geometry laser. The geometry laser measured the distance from the laser head to each scan point and calculated the x-, y- and z-coordinates

Table 3.4: Experiment 2: 3D alignment quality for Skull A (* measurement view used to define global 3D coordinate system)

Measurement View	Alignment Quality (mm)		
	Top Laser	Left Laser	Right Laser
Top (*)	0	0.7	0.4
Bottom	0.9	0.3	0.5
Right	0.8	0.5	0.7
Left	1.0	0.6	0.5
Anterior	0.9	0.6	0.6
Posterior	0.9	0.3	0.6

Table 3.5: Experiment 2: 3D alignment quality for Skull B (* measurement view used to define global 3D coordinate system)

Measurement View	Alignment Quality (mm)		
	Top Laser	Left Laser	Right Laser
Top	0.1	0.2	0.3
Bottom	0.3	0.3	0.4
Right	0.3	0.3	0.3
Left	0.3	0.2	0.3
Anterior (*)	0	0.1	0.4
Posterior	0.4	0.3	0.4

using this measurement and the current mirror angles. Scan points covering areas with large curvatures or detailed features were inspected to ensure convergence of all three lasers. If the three lasers did not converge to the given scan point that point was disabled and not included in the data acquisition scan.

This experiment used a sinusoidal function as an input signal, which allowed the vibration pattern over the entire surface of the skull to be visualized at discrete frequencies. A total of 13 frequencies were measured within the frequency range of 100–20000 Hz. Similar to Experiment 1 in Section 3.1, different acquisition settings were used for three different ranges of frequencies. The frequency ranges and the corresponding acquisition and channel settings are listed in Table 3.6 and Table 3.7, respectively, for both Skull A and Skull

B. The number of FFT lines for Skull A were chosen such that the acquisition time for each scan point remained the same. Due to minor hardware limitations, the maximum number of FFT lines across all three frequency ranges was limited to an adequate value of 51200 for the Skull B experiment. Using the first measurement view, the generator and channel settings were determined for each frequency range such that a balance was achieved between a high generator signal to increase SNR and low channel ranges to increase signal resolution.

Table 3.6: Experiment 2: Acquisition settings

Skull	Frequency Range (kHz)	Bandwidth (kHz)	FFT Lines	Sample Time (s)	Sensitivity (mm/s/V)	Generator Amplitude (V)
A	Low: 0.1–5	5	51,200	10.24	0.2	0.1
	Mid: 5–10	10	102,400	10.24	1	0.2
	High: 10–20	20	204,800	10.24	5	0.3
B	Low: 0.1–5	5	51,200	10.24	0.2	0.075
	Mid: 5–10	10	51,200	5.12	1	0.15
	High: 10–20	20	51,200	2.56	2	0.2

Table 3.7: Experiment 2: Channel settings

Skull	Channel	Quantity	Range (V)		
			Low	Mid	High
A	Vib 3D	Velocity	10	10	10
	Ref21	Voltage	10	10	10
	Ref22	-	-	-	-
B	Vib 3D	Velocity	10	10	10
	Ref21	Voltage	1	1	1
	Ref22	Force	1	1	1

Before beginning data acquisition in each of the subsequent measurement views, the signal-to-noise ratio (SNR) was verified using the same acquisition settings for each frequency range. The SNR for each measurement view and at each frequency range were found to be within 20–60 dB. All 13 scans, one for each frequency measured, were ran in the same measurement view before reorienting the skull and aligning the next view. The data for each scan was saved in the proprietary binary format Scan Data (*.svd file) resulting in a total of 13 *.svd files for each measurement view. An additional 41 frequencies were measured in the posterior measurement view using the same acquisition and channel settings listed in Table 3.6 and Table 3.7, respectively. The 41 frequencies were evenly spaced from 6–20 kHz (a 350 Hz spacing).

A custom Visual Basic[®] macro was developed that greatly reduced the time to run multiple scans by eliminating the need for the user to manually step through each frequency. For every frequency measured, the macro loaded a proprietary binary format Settings File (*.set file) into the PSV software, ran a complete scan of all active scan points in the grid, and saved the data to an *.svd file. Included in these settings files were the 2D and 3D alignment, the grid of scan points including the coordinate values associated with each point, and the acquisition and channel settings. A second Visual Basic[®] macro was created that automated the generation of the settings files in each frequency range. The settings and scan macros are included in Appendix B

3.2.3 *Preliminary Data Post-Processing*

To view and manipulate the data the PSV 8.6 software was set to "Presentation Mode". For each of the 13 frequencies measured, the 3D geometry and vibratory response contained in the *.svd files of the six individual measurement views were stitched together in a combined file. This was a straightforward process since the same, carefully predefined coordinate system was applied to all the measurement views, and the same acquisition and channel settings were used in each measurement view at a given frequency. Since many of the scan points in the individual measurements shared the same indices, new values were assigned to ensure all scan points in the combined file had unique indices. The combined files were saved in the same format as the individual measurements, i.e. *.svd.

A frequency band corresponding to the measurement frequency was defined for each

combined file. Since the skull was driven with a pure sine wave, the start and end frequencies for the band definition were simply the measurement frequency of the combined file, resulting in a bandwidth of 0 Hz. By applying a band definition, the magnitude and phase data for each scan point was extracted from the FFT of the recorded time signal at the measurement frequency. Since the driving signal was also used as a trigger signal, the phase relationship between all scan points was well defined and thus it was possible to animate the vibration pattern over the entire surface of the skull using this extracted data. The software calculated the phase-dependent instantaneous magnitude at each scan point from the following equation

$$A(\phi) = A_o \sin(\phi + \phi_o) \quad (3.5)$$

where A_o is the peak amplitude and ϕ_o is the phase offset (Polytec GmbH, n.d.b; Osten, 2007). The animation for a complete period was created in the software by cycling the phase ϕ from -180° to 180° , calculating the instantaneous magnitude of vibration at 10° intervals.

3.3 Experiment 3

The third experiment compared the vibration of the outer surface of the skull to the inner surface at high frequencies.

3.3.1 *Skull Prep*

Skull B prepared as per sections 3.1.1 and 3.2.1 was used for this experiment. Retroreflective tape was applied to the measurement surfaces to increase the optical signal level of the vibrometer controller (Figure 3.3a and Figure 3.3b).

3.3.2 *Setup*

The inner and outer surfaces were measured at the same location on the skull. The inner surface was measured through the foramen magnum (the opening in the occipital bone at

the base of the skull allowing passage of the spinal cord, shown in Figure 3.3b), which limited the measurement area to the top of the skull. This was adequate since the cranial vault was the region of interest. The scanning 3D LDV used in Experiment 2 was used, since the focal length of this laser was not fixed and could be focused to the inner surface through the foramen magnum. The PSV 8.6 software laser was used to interface with the LDV, and to acquire and interpret the data. The LDV was set to 1D mode, thereby only using the top or central laser head. Since only the magnitude and phase of the surface velocity perpendicular to the surface was required, this mode was adequate. The skull was mounted on the elastic suspension system in Figure 3.2 in such a way that at the measurement point the surface was as perpendicular to the laser beam as possible. The measurement point on the outer surface was measured first. The inner measurement point was located by using the mounting screw shown in Figure 3.3a as a reference point. The skull was driven with a burst chirp signal from 10–20 kHz that was generated in the PSV software and amplified by an external audio amplifier. The generated signal was used as a trigger for data acquisition. Table 3.8 lists the software settings used for data acquisition. Since only the high frequencies were of interest for this measurement only one frequency range was required.

Table 3.8: Experiment 3: Settings

Settings	Value	Units
Frequency Range	10–20	kHz
Complex Averages	100	-
Bandwidth	25	kHz
FFT Lines	12800	-
Channels:		
Vib Top Range	3.162	V
Ref 21 Range	3.162	V
Burst Chirp Signal:		
Amplitude	0.2	V
Start Frequency	8	kHz
End Frequency	22	kHz

3.3.3 Preliminary Post-Processing

The H2 frequency response functions for the inner and outer measurements were exported from the PSV software to an ASCII file. An explanation of how the software calculates the H2 frequency response is given in section 3.1.3. The coherence was also exported from the PSV software to an ASCII file (Polytec GmbH, n.d.b). The software calculates the coherence function COH using the H1 and H2 frequency response functions given by (3.1) and (3.1), respectively, as per the following equation

$$\text{COH}_{VR_i} = \frac{H1_{VR}}{H2_{VR}} \quad (3.6)$$

This provides a measure of the power of the output signal generated by the input signal. If (3.6) is 1, then the output signal is generated entirely by the input signal. If (3.6) is 0, then none of the output signal is generated by the input signal.

CHAPTER 4

RESULTS AND DISCUSSION

The following section presents the results of the experiments outlined in Chapter 3 and gives a discussion of the findings. The 3D vibration patterns obtained using the 3D scanning LDV are discussed first, followed by the findings on wave propagation in the skull.

4.1 3D Vibration Patterns

The vibration pattern over the 3D surface of the skull was animated using the combined *.svd files generated as per Section 3.2.3. Figure 4.1 and Figure 4.2 show screenshots from the animated 3D velocity field of surface vibrations of Skull A and Skull B, respectively, for three representative frequencies of the thirteen measured. A wireframe of the undeformed skull is included in each figure for reference. The deformations of the triangular surface meshes are proportional to the measured vibratory response of the skull in terms of magnitude and direction at the individual scan points, though the magnitude of the displayed deformations are greatly exaggerated for visualization purposes.

At 500 Hz there is little deformation and the skull moves nearly as one mass, displaying quasi-rigid body motion. The term "quasi" is used here as there are small localized deformations at the excitation site. At 3000 Hz distinct deformations are observed with major structures of the skull moving out of phase with one another. Only three or four wavelengths are present over the entire surface of the skull, which implies that below 3000

Hz the number of free resonances is on the same order. At 16000 Hz significantly more deformations are present with many wavelengths covering the surface of the skull. A distinct "egg-carton" pattern is observed along the cranial vault of the skull, which implies a uniform wavelength in this region. Figure 4.3 illustrates the wave pattern in 2D at 16000 Hz for the posterior view of the skull. Again, even spacing between peaks and troughs is apparent with wavefronts propagating away from the excitation site (the Baha[®] is located on the left side of the skull). A uniform wavelength implies relatively consistent material and geometric properties within the posterior region of the skull.

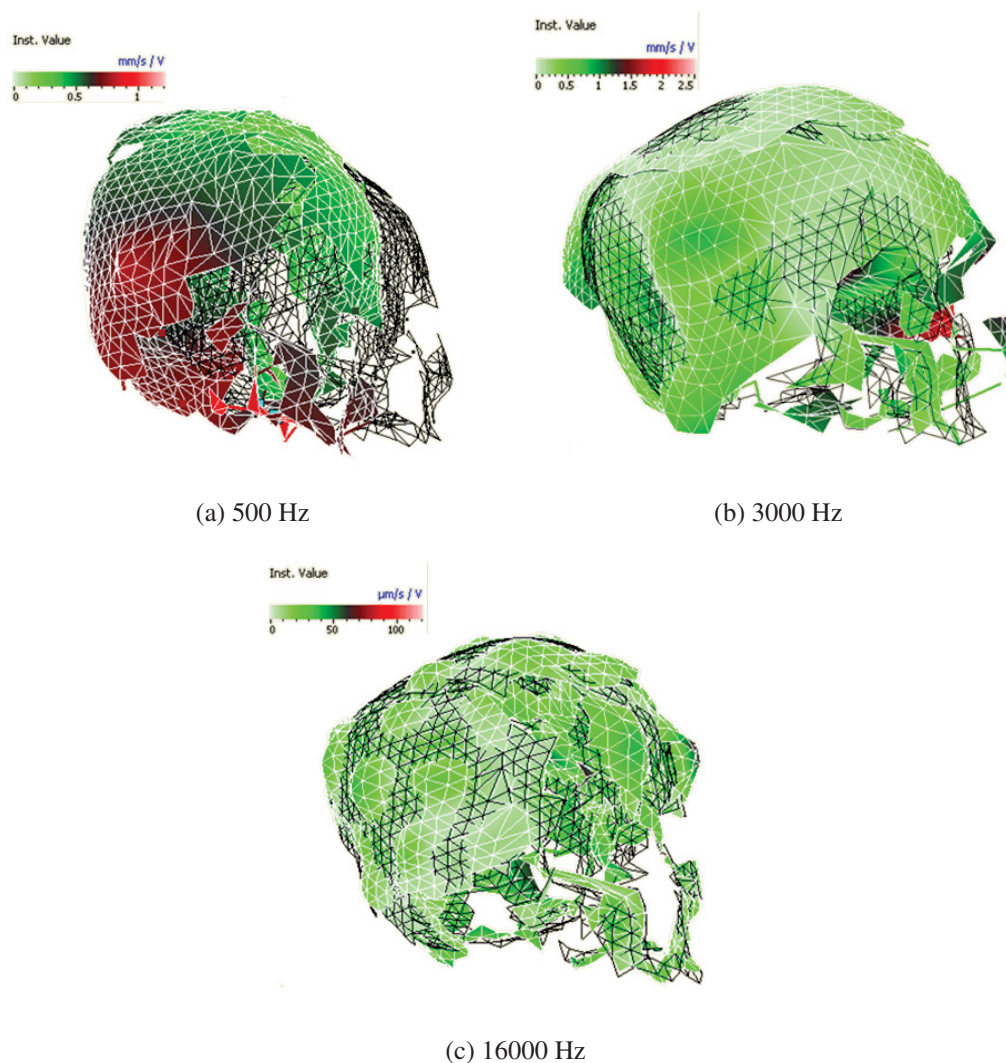


Figure 4.1: 3D velocity fields for Skull A at three representative frequencies. The undeformed skull is given by the wireframe mesh.

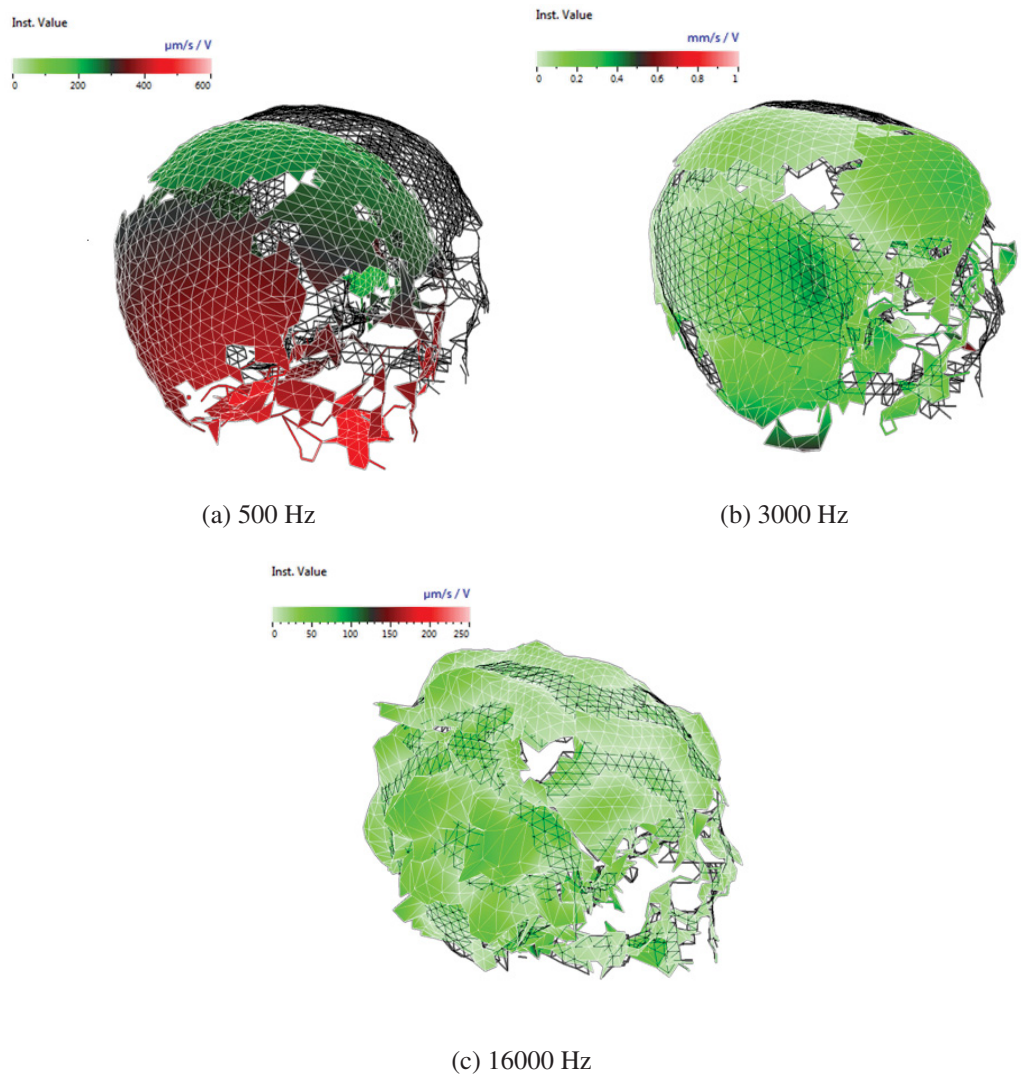
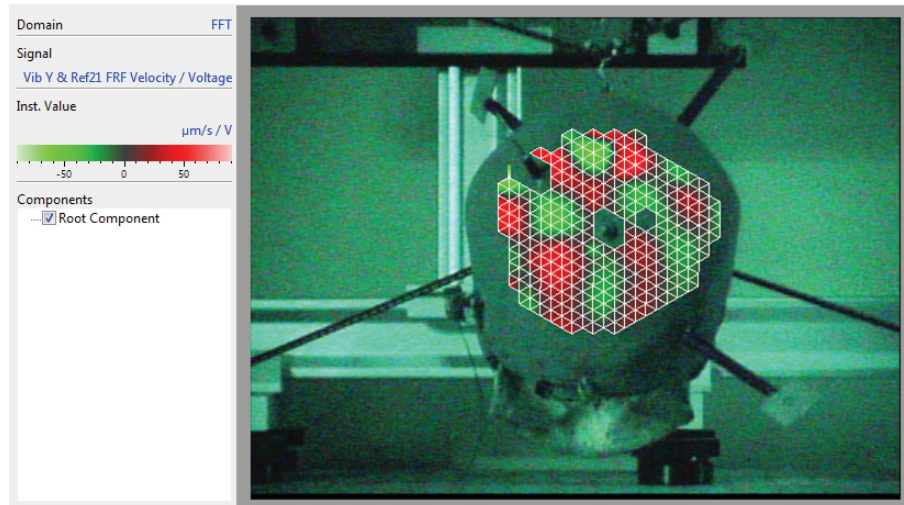
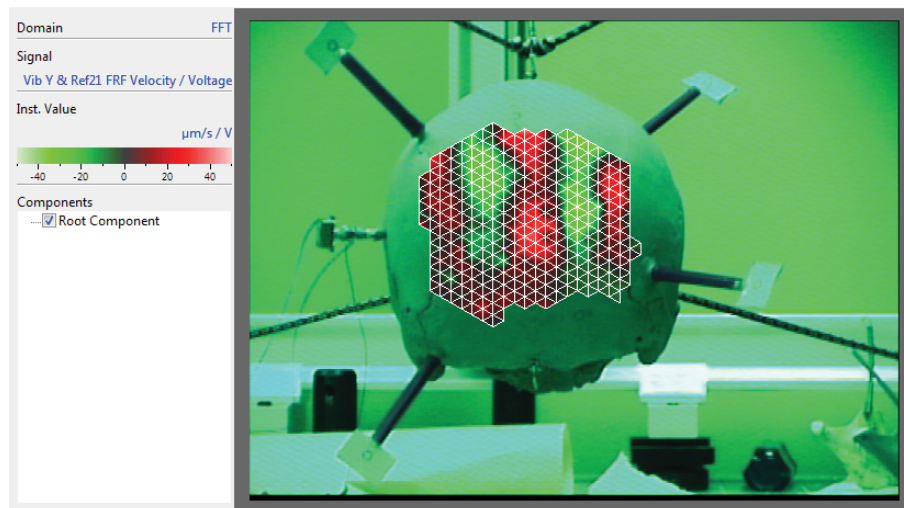


Figure 4.2: 3D velocity fields for Skull B at three representative frequencies. The undeformed skull is given by the wireframe mesh.



(a) Skull A



(b) Skull B

Figure 4.3: 2D Velocity Field at 16000 Hz.

4.2 Wave Propagation in Skull Bone

The magnitude of the surface velocity at each experimental site in Experiment 1 was calculated by taking the root sum square of the three non-collinear velocity components. These surface velocity magnitudes were then averaged over the five experimental sites. The admittance was calculated by normalizing the average surface velocity to the input force. The force was obtained by multiplying the acceleration of the Baha[®] casing with the effective mass of the Baha[®] motor. This method of measuring input force was validated previously by Dr. Robert B. Adamson in the S.E.N.S.E. Laboratory at Dalhousie

University using a TU1000 skull simulator (Håkansson & Carlsson, 1989). A Baha[®] motor was attached to the simulator and driven with a swept sinusoidal function from 100–30000 Hz. The velocity of the Baha[®] casing was measured with an LDV and the force F calculated from the following equation

$$F = 2\pi f v_l m_b \quad (4.1)$$

where f is the frequency, v_l is the linear velocity, and m_b is the effective mass of the Baha[®] motor. This calculated force was compared with the measured force from the skull simulator. The effective mass m_b was used as a fitting parameter and found to be 5.53 g. Figure 4.4 shows the measured skull simulator force and the calculated LDV force with a 5.53 g effective mass. The discrepancy at high frequency is expected since the skull simulator is only reliable up to 10 kHz (Håkansson & Carlsson, 1989). Using this validated effective mass and the LDV acceleration data, the input force for Skull A and Skull B were calculated and are shown in Figure 4.5.

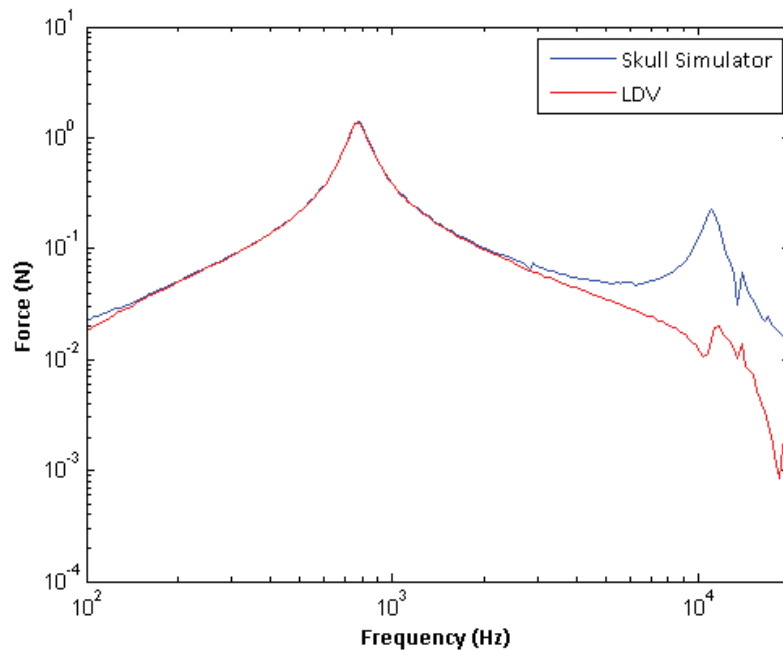
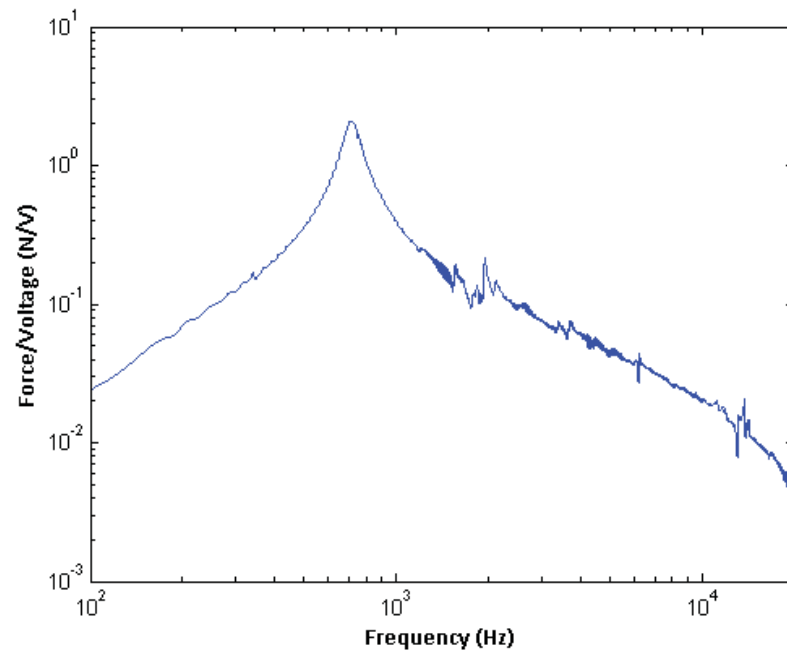
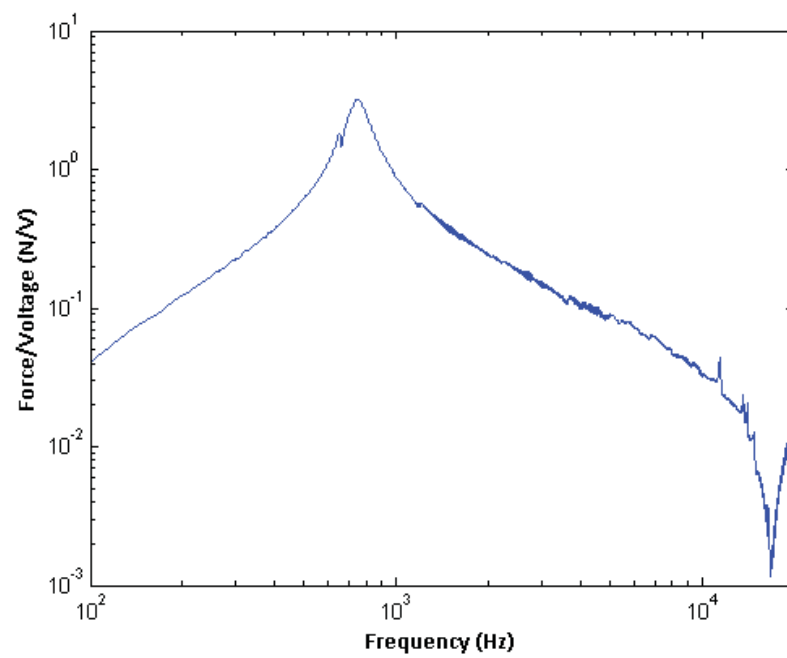


Figure 4.4: TU1000 skull simulator force data compared force calculated from LDV velocity data. The effective mass m_b was used as a fitting parameter and found to be 5.53 g.



(a) Skull A



(b) Skull B

Figure 4.5: Input forces calculated using a 5.53 g effective mass.

Figure 4.6 shows the admittance plots in log-log scale for (a) Skull A and (b) Skull B (solid-lines). The MATLAB[®] code used to calculate the force and admittance are given in Appendix A.

Below 1000 Hz, the admittance of each skull appears to follow a power law with an exponent of negative one, which is indicative of a point-mass. The admittance of a point-mass is derived by first considering the equation for force:

$$\begin{aligned} F &= mv\omega \\ &= mv(2\pi f) \end{aligned} \quad (4.2)$$

where m is the point-mass and ω is the angular velocity. Rearranging (4.2) gives

$$\begin{aligned} \text{Admittance} &= \frac{v}{F} \\ &= \frac{1}{2\pi m f} \end{aligned} \quad (4.3)$$

$$\text{Admittance (dB)} = 20 \log \frac{1}{2\pi m f} \quad (4.4)$$

The point-mass behaviour observed in Figure 4.6 is confirmed by the dotted-line in each plot, which is the point-mass admittance given by (4.4) with m equal to the measured mass of the respective skull. The measured masses of Skull A and Skull B were 440.27 g and 651.78 g, respectively. This behaviour is also observed at low frequencies in Figure 4.1a and Figure 4.2a. These findings confirm that at low frequencies the skull can be treated as a quasi-rigid body, which is consistent with other studies in the literature (Håkansson *et al.*, 1986, 1994).

Above 1000 Hz, distinct resonant peaks are observed in the admittance data, which is consistent with the vibratory patterns at 3000 Hz shown in Figure 4.1b and Figure 4.2b, where large wavelength deformations are present. The averaging over the five experimental sites accentuates these resonances while reducing the antiresonances. The average quality (Q) factors associated with the resonant peaks were 17.8 and 14.0 for Skull A and Skull B, respectively. The resonances were identified and enumerated for each data set to obtain a coarse relationship between mode number and frequency.

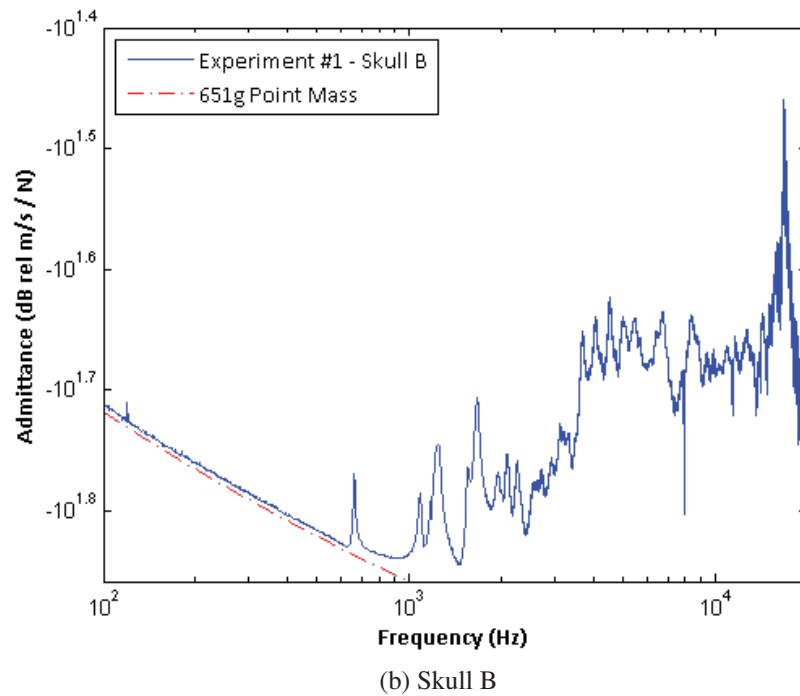
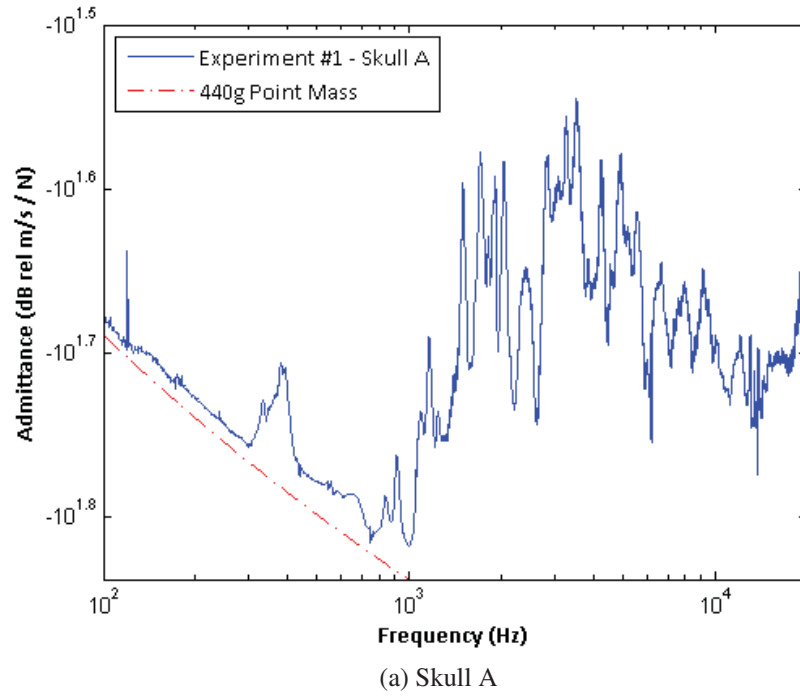


Figure 4.6: The admittance of (a) Skull A and (b) Skull B (solid-lines), and the admittance of a point-mass of (a) 440 g and (b) 651 g (dotted-line), which are equivalent to the measured masses of the respective skulls.

It should be noted that the distinct peak observed at approximately 380 Hz in Figure 4.6a was not included in the identification of resonant frequencies as it was attributed to the resonance of the linear spring securing the mandible to the rest of Skull A. This is confirmed in Figure 4.7, which shows the admittance for a burst chirp from 100 - 5000 Hz with the mandible attached (blue line) and without the mandible attached (green line). When the mandible is removed the resonance at 380 Hz is no longer present.

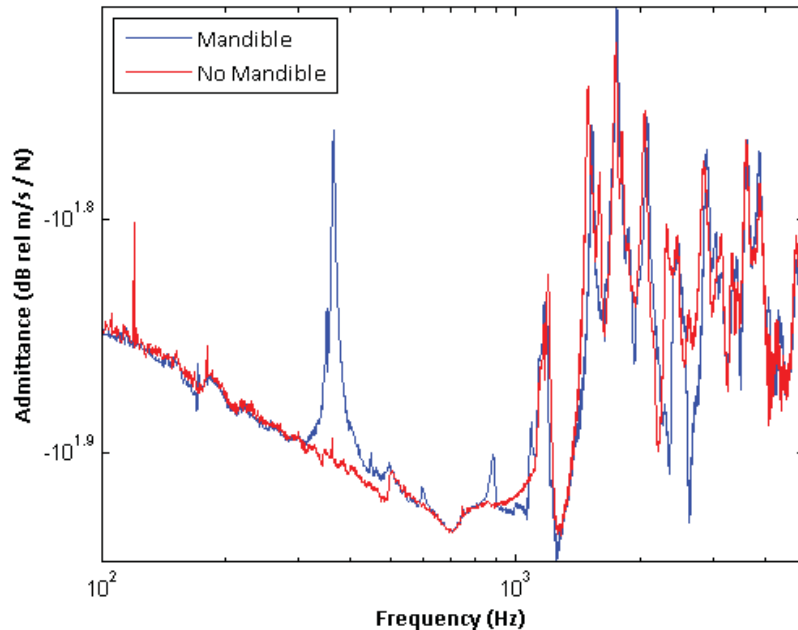
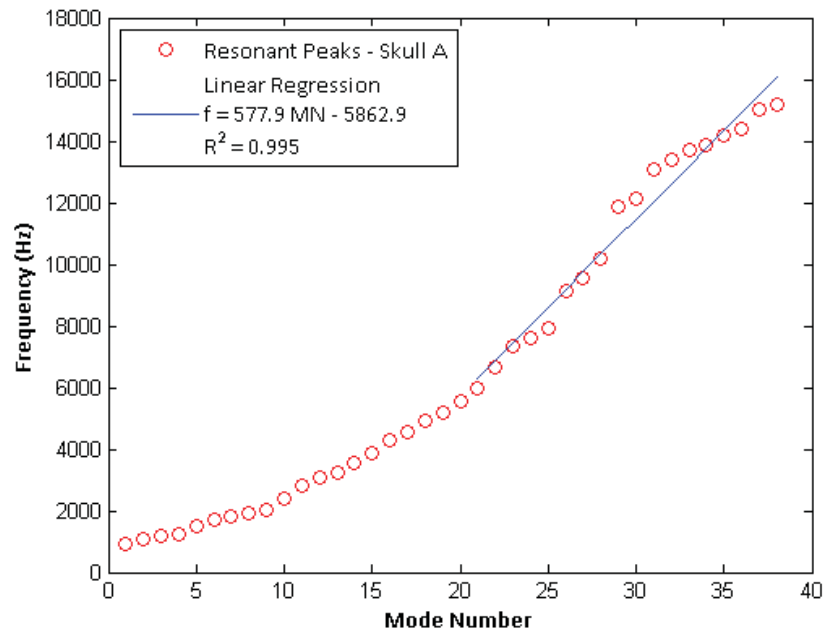


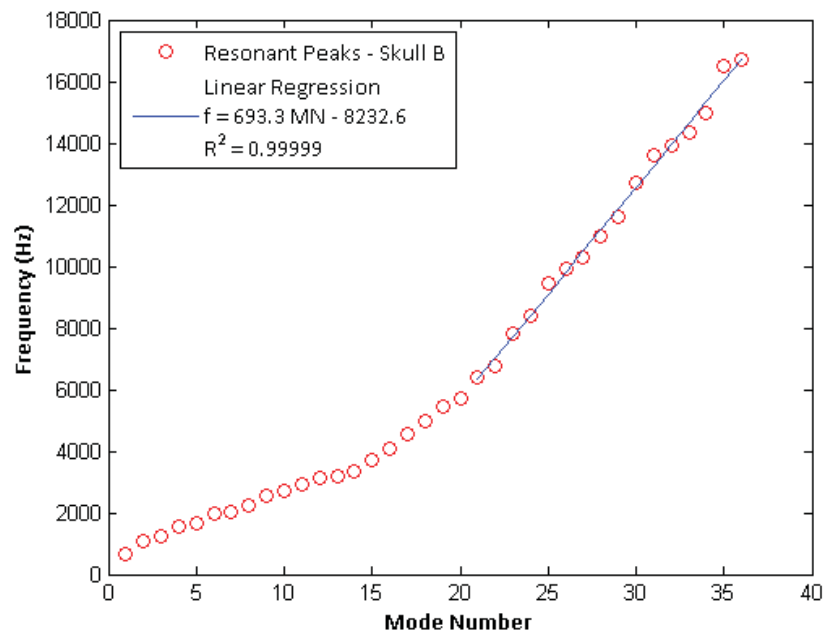
Figure 4.7: The admittance for Skull A from 100 - 5000 Hz with the mandible attached (blue line) and without the mandible attached (red line). The resonance observed with the mandible attached at approximately 380 Hz is a result of the two linear springs securing the mandible to the rest of the skull.

Figure 4.8 plots mode number versus resonant frequency. At high frequencies, above 6000 Hz, both resonance data agreed well with linear fits (solid-lines). The R^2 values associated with the linear fits to data from Skull A and Skull B were 0.995 and 0.99999, respectively.

These results indicate that at high frequencies, above 6000 Hz, frequency is linearly dependent on mode number. Since the identified resonant frequencies were assigned increasing numbers in the order which they appeared, the mode number is inversely proportional to the wavelength. Consequently, the mode number is proportional to the wave number and has the same functional dependence on frequency, in other words, the dispersion relationship. A linear dispersion relationship, or non-dispersive behaviour,



(a) Skull A



(b) Skull B

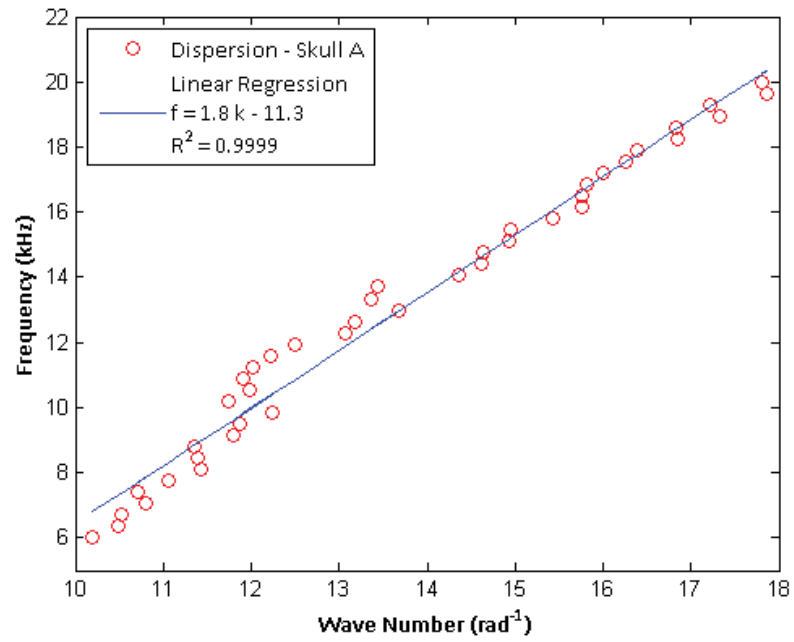
Figure 4.8: Increasing mode number plotted against the corresponding resonant frequencies. The solid lines show the linear fits with R^2 values of 0.995 and 0.99999 for Skull A and Skull B, respectively.

is indicative of the extensional zero-order Lamb wave mode that occurs in plates. The skull can be treated as a plate only at the high frequencies of human hearing where the wavelength is much smaller than the radius of curvature. Additionally, the zero-order Lamb wave modes only exist when the dimensionless quantity $\frac{\omega h}{c_2}$ is much less than one. For the upper frequency limit of human hearing (20000 Hz) and reasonable parameters of a human skull (Table 2.1), the dimensionless quantity is 0.1, and thus it is reasonable to assume that Lamb waves exist in the skull at high frequencies but within the zero-order limit.

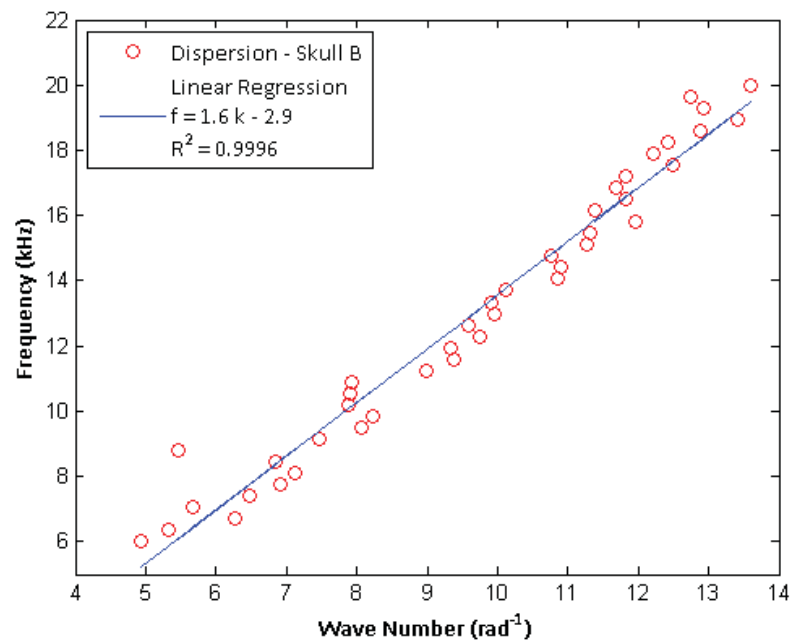
Experiment 1 gives a relatively coarse measure of the dispersion since resonant peaks were manually identified and it is possible that degenerate modes were included. A higher fidelity measure of the dispersion relationship was obtained from the additional data set from Experiment 2 that measured a total of 41 frequencies between 6–20 kHz in the posterior view (see section 3.2). The posterior view included the occipital bone and the posterior regions of the left and right parietal bones. The following data manipulation was conducted by Dr. Robert B. Adamson in the S.E.N.S.E. Laboratory at Dalhousie University. Additional details of this analysis than those given here are provided in Appendix C.

The posterior region was chosen for this analysis since the wave patterns observed at high frequencies showed a relatively consistent wavelength within this region (Figure 4.3). Thus it is reasonable to assume that each vibration pattern was generated by the interference of many waves, traveling in different directions around the skull but all having the same wavelength. The wave number k , given by the magnitude of the wave vector $k = |\vec{k}| = \frac{2\pi}{\lambda}$, would also be the same for each propagating wave. A numerical optimization routine discussed in Appendix C was used to determine the wave number that best recreated the velocity field at each frequency. The resulting dispersion relationship is shown in Figure 4.9 for each skull. A linear regression fit yields R^2 values of 0.9999 and 0.9996 for Skull A and Skull B, respectively, indicating non-dispersive behaviour. This result is indicative of the extensional zero-order Lamb wave mode, where particle motion is symmetric about the midplane of the plate.

A 3D vectorial representation of the velocity field at a representative frequency of 10550 Hz is shown in Figure 4.10. Distinct regions of normal displacement surrounded by regions of tangential displacement are observed, with the tangential vectors pointing to regions



(a) Skull A



(b) Skull B

Figure 4.9: The dispersion relationship from Experiment 2. The solid-lines show the linear fits with R^2 values of 0.9999 and 0.9996 for Skull A and Skull B, respectively.

of outward normal displacement. When the normal component is at a maximum, the tangential component is at a minimum, and vice versa. As illustrated by the particle motion depicted in Figure 2.2, this behaviour is also indicative of Lamb waves, however is characteristic of surface plate waves as well, where the particle motion also follows an elliptical path.

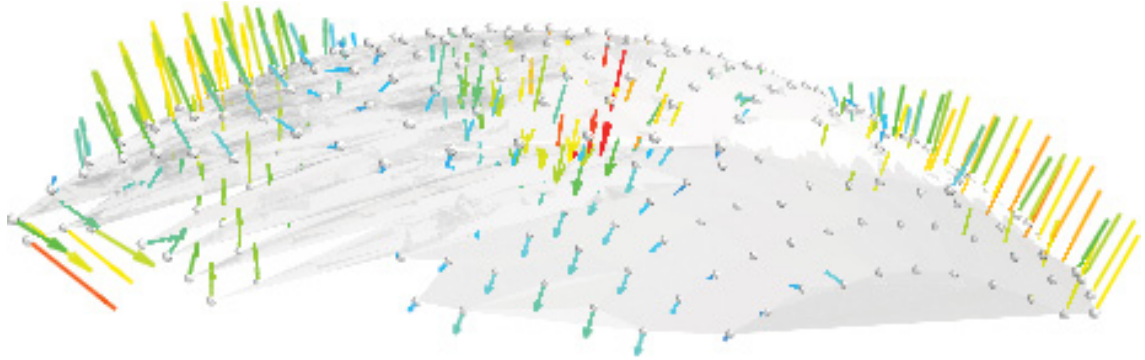


Figure 4.10: The 3D velocity field at 10550 Hz in the posterior view of the skull. The vectors indicate direction and relative magnitude of the surface velocity.

To rule out surface waves and confirm the presence of extensional zero-order Lamb waves, the displacement of the outer and inner surface of the skull must be of similar magnitudes and symmetrical about the midsurface of the skull as shown in Figure 2.2a. Figure 4.11 shows the absolute value of the phase difference between the inner and outer surfaces of a point on the skull obtained in Experiment 3. The majority of points center around 180° . The large deviations from 180° that occur mainly at the low end of the frequency range correspond to troughs in the coherence (Figure 4.12), which in turn correspond to resonances and antiresonances in the H2 frequency response function (Figure 4.13). These common peaks and troughs are indicated by numbered boxes in each of the figures and occur at (1) 11340 Hz, (2) 11540 Hz and (3) 12850 Hz.

Figure 4.11 indicates that the inside and outside surfaces of the skull are moving anti-symmetrically to one another about the midplane of the skull. This suggests the flexural zero-order Lamb wave mode, which cannot be the case since the wave number would have to depend on the square-root of frequency. The results from Experiment 3 also rule out surface waves in plates (i.e. Rayleigh or Love waves) since the motion of the inner and outer surfaces are of comparable magnitudes (Figure 4.13).

Instead, a spherical shell model was considered to describe the wave propagation in the

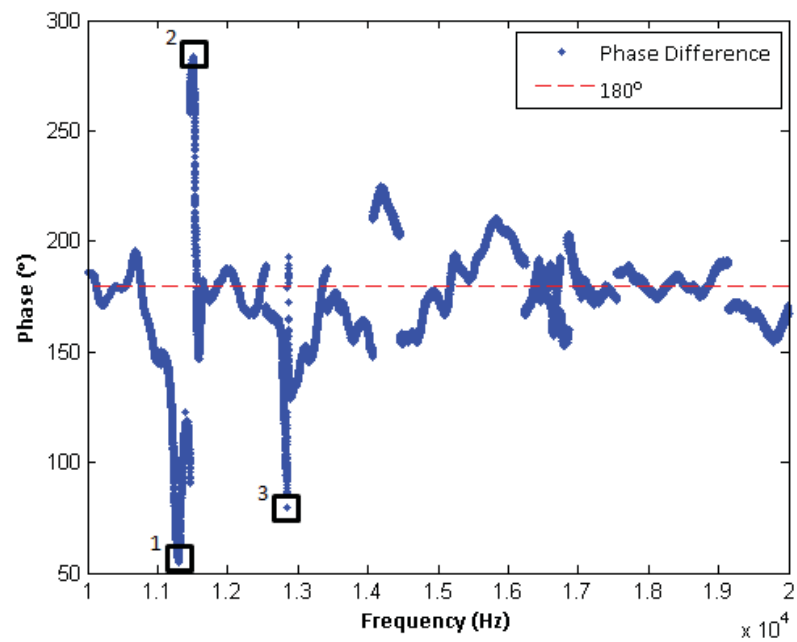


Figure 4.11: The absolute value of the phase difference between the inner and outer surface of the skull.

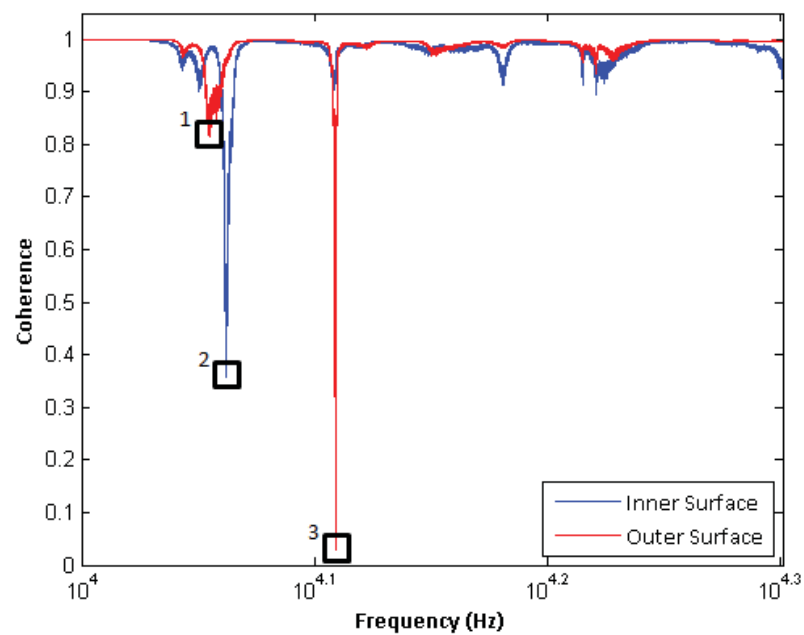


Figure 4.12: Coherence for the inner (red line) and outer (blue line) surfaces. Troughs correspond to deviations in the phase difference from 180°

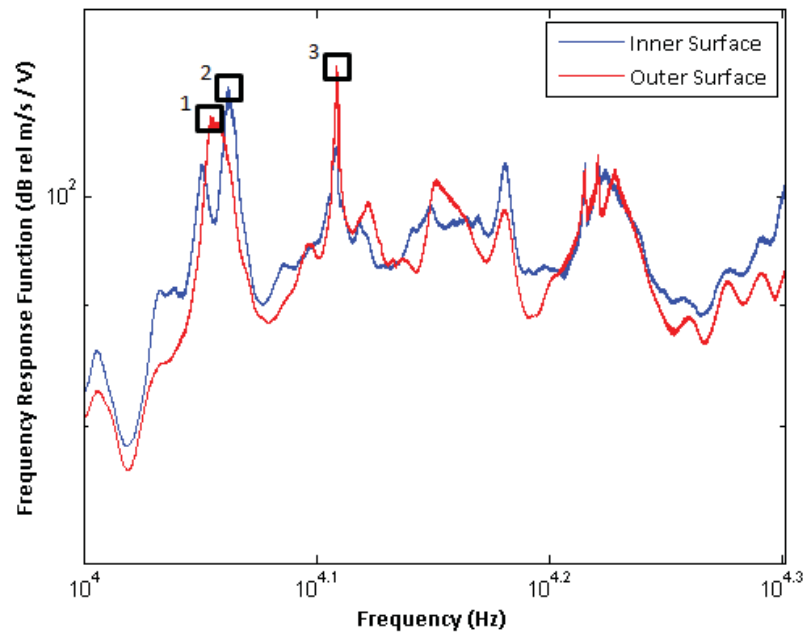
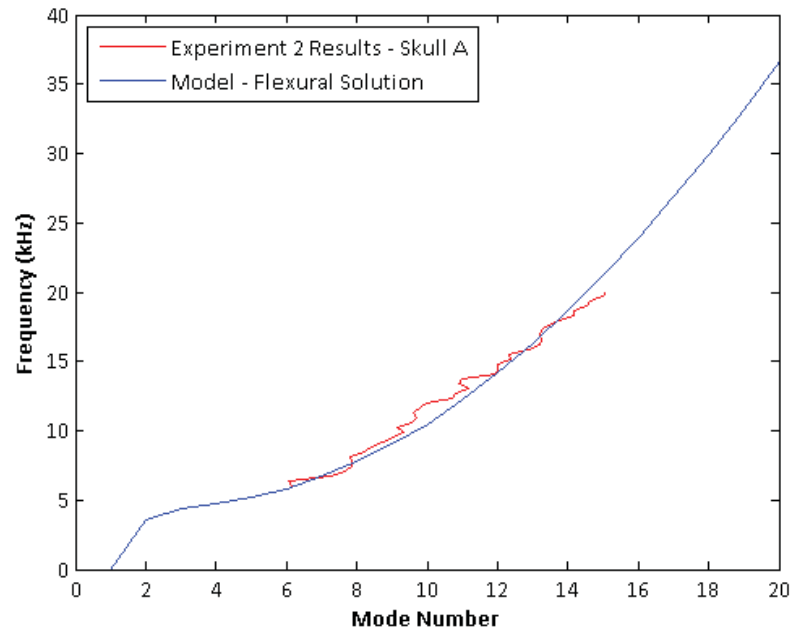
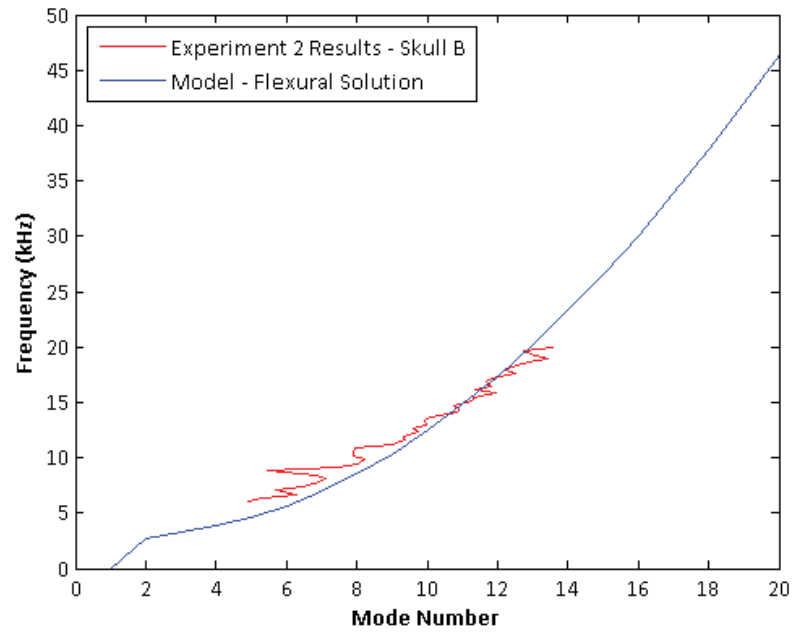


Figure 4.13: The H2 frequency response function for the inner (red line) and outer (blue line) surfaces. Resonances and antiresonances correspond to deviations in the phase difference from 180° .

skull. The data from Experiment 2 was compared with the solution to the vibration problem of spherical shells presented in section 2.3. The dimensionless frequency Ω was converted to real frequencies as per equation 2.32. The wave numbers from the experimental results were converted to mode numbers by calculating the number of wavelengths that fit into the circumference of the respective skull. The radius of the spherical surface fit to each skull's data was used to calculate the frequencies and circumference of the respective skull. A constrained, non-linear least squares optimization scheme included in Appendix D was used to determine the remaining geometric and material parameters that best fit the model to the experimental data of Experiment 2. The Young's modulus, Poisson's ratio, density and thickness were all varied within reasonable limits for a human cranial bone (McElhane *et al.*, 1970). Figure 4.14 shows the flexural branch of the spherical shell model fit to the data from Experiment 2. The fitted geometric and material parameters are listed in Table 4.1. The spherical shell model gives a good approximation of the frequency response of the skull between 6000 and 20000 Hz.



(a) Skull A



(b) Skull B

Figure 4.14: Dispersion relationship from Experiment 2 fit to flexural branch spherical shell model using a non-linear least squares optimization.

Table 4.1: Geometric and material parameters used to fit Experiment 2 data to flexural branch of spherical shell model.

(a) Skull A			(b) Skull B		
Parameter	Symbol	Value	Parameter	Symbol	Value
Young's modulus	E	5.5 GPa	Young's modulus	E	5.5 GPa
Poisson's ratio	ν	0.31	Poisson's ratio	ν	0.33
density	ρ	1506 kg/m ³	density	ρ	1600 kg/m ³
thickness	h	5 mm	thickness	h	7.9 mm

CHAPTER 5

CONCLUSIONS

The vibratory response of dry human skulls was investigated through three experiments using laser Doppler vibrometry to better understand the mechanisms of bone conduction. Two wave theories were considered to model the behaviour observed in the experimental results; Lamb plate waves and a spherical shell model.

First, the admittance of two skulls was obtained using a high spectral density experiment. At low frequencies the admittance followed that of a point-mass, indicating rigid body behaviour. Above 900 Hz, distinct resonances and antiresonances were observed. These results were consistent across the two skulls and were confirmed by a second experiment that measured the surface velocity of the same two skulls at 13 discrete frequencies. The result was a 3D animation of the vibratory pattern over the entire surface of the skull at each of the 13 frequencies.

An additional dataset that measured the velocity field at 41 frequencies in the posterior region of the skull was used to determine the dispersion relationship for each skull. The results indicated non-dispersive behaviour, which is consistent with extensional Lamb waves in a plate. However, this result was not confirmed by Experiment 3, which measured the vibratory response of the inner and outer surface at a single point on the skull. The results showed instead that movement of the inner and outer surfaces was antisymmetric about the midplane of the skull. If a Lamb plate wave theory is considered, this result eliminates the presence of the extensional mode and instead suggests the flexural mode. However, since the dispersion relationship was not dependent on the

square-root of frequency, flexural Lamb plate waves also did not describe this behaviour. Antisymmetric motion of the inner and outer surfaces of the skull with respect to the midplane is consistent with a closed spherical shell model. Upon fitting the spherical shell model to the experimental dispersion relationship, the flexural branch of the spherical shell model proved to be a reasonable indicator of the frequency response of the human skull within the range of human hearing.

Therefore, the Lamb plate wave theory cannot be used to describe wave propagation in the posterior region of the skull at high frequencies. The implication of this finding is significant given that the type of wave heavily influences the wave propagation characteristics. A spherical shell model, on the other hand, showed better agreement with the experimental results. Through the 3D vibratory responses and dispersion relationships obtained from this work, further insight into the propagation of waves in the skull was achieved. A better understanding of wave propagation and other mechanisms of bone conduction will aid in improving existing bone anchored hearing prostheses and greatly benefit the advancement of new bone conduction hearing devices.

A recommendation for generating 3D vibration patterns in the future is to measure more than six views. Due to the complex topography of the skull, many of the outer most grid points in a view were removed from the dataset since all three laser beams were unable to converge to a single a point at these locations. This created small gaps between the measurement views after stitching the velocity fields together. Acquiring data from additional measurement views would recreate a smoother geometry of the skull, albeit at greater experimental effort.

Another recommendation for future work is to obtain high spectral density datasets from additional regions of the skull to determine if the dispersion relationship changes with location. The motion of the inner surface with respect to the outer surface should also be investigated at these locations to gain a more thorough understanding of the wave propagation in these regions. Accessing the inner surface of the skull at these additional locations will not be possible through the foramen magnum. A possible alternative would be to drill a small hole on the opposite side of the skull to the region being investigated.

REFERENCES

- Amirkulova, F. A. (2011). *Dispersion relations for elastic waves in plates and rods*. Master's thesis, Rutgers, The State University of New Jersey.
- Arlinger, S. D., Kylén, P., & Hellqvist, H. (1978). Skull distortion of bone conducted signals. *Acta Oto-Laryngologica*, 85(5-6), 318–323.
- Baker, W. E. (1961). Axisymmetric modes of vibration of thin spherical shell. *The Journal of the Acoustical Society of America*, 33(12), 1749–1758.
- Brent, R. P. (1973). *Algorithms for Minimization without Derivatives*. Englewood Cliffs, NJ: Prentice-Hall.
- Cochlear Ltd. (2011). Cochlear - implants for children and adults.
URL <http://www.cochlear.com>
- Eeg-Olofsson, M., Stenfelt, S., Tjellström, A., & Granström, G. (2008). Transmission of bone-conducted sound in the human skull measured by cochlear vibrations. *International Journal of Audiology*, 47(12), 761–769.
- Eichorn, D. H., & Bayley, N. (1962). Growth in head circumference from birth through young adulthood. *Child Development*, 33(2), 257–271.
- Engin, A. E., & Liu, Y. K. (1970). Axisymmetric response of a fluid-filled spherical shell in free vibrations. *Journal of Biomechanics*, 3(1), 11–22.
- Franke, E. K. (1956). Response of the human skull to mechanical vibrations. *The Journal of the Acoustical Society of America*, 28(6), 1277–1284.
- Hoyer, H.-E., & Dörheide, J. (1983). A study of human head vibrations using time-averaged holography. *Journal of Neurosurgery*, 58, 729–733.
- Håkansson, B., Brandt, A., Carlsson, P., & Tjellström, A. (1994). Resonance frequencies of the human skull in vivo. *The Journal of the Acoustical Society of America*, 95(3), 1474–1481.
- Håkansson, B., & Carlsson, P. (1989). Skull simulator for direct bone conduction hearing devices. *Scandinavian Audiology*, 18(2), 91–98.
- Håkansson, B., Carlsson, P., Brandt, A., & Stenfelt, S. (1996). Linearity of sound transmission through the human skull in vivo. *The Journal of the Acoustical Society of America*, 99(4), 2239–2243.
- Håkansson, B., Carlsson, P., & Tjellström, A. (1986). The mechanical point impedance of the human head, with and without skin penetration. *The Journal of the Acoustical Society of America*, 80(4), 1065–1075.

- Håkansson, B., Tjellström, A., & Rosenhall, U. (1984). Hearing thresholds with direct bone conduction versus conventional bone conduction. *Scandinavian Audiology*, 13(1), 3–13.
- Huber, A. M., Sequeira, D., Breuninger, C., & Eiber, A. (2008). The effects of complex stapes motion on the response of the cochlea. *Otology & Neurotology*, 29, 1187–1192.
- Junger, M. C., & Feit, D. (1972). *Sound, Structures, and Their Interaction*. The MIT Press, Cambridge, Massachusetts.
- Kalnins, A. (1964). Effect of bending on vibrations of spherical shells. *The Journal of the Acoustical Society of America*, 36(1), 74–81.
- Khalil, T. B., Viano, D. C., & Smith, D. L. (1979). Experimental analysis of the vibrational characteristics of the human skull. *Journal of Sound and Vibration*, 63(3), 351–376.
- Khanna, S. M., Tonndorf, J., & Queller, J. E. (1976). Mechanical parameters of hearing by bone conduction. *The Journal of the Acoustical Society of America*, 60(1), 139–154.
- Kirikae, I. (1959). An experimental study on the fundamental mechanism of bone conduction. *Acta Otolaryngol*, 145, 1–111.
- Lamb, H. (1917). On waves in an elastic plate. *Proceedings of the Royal Society A*, 93, 114–128.
- McElhaney, J. H., Fogle, J. L., Melvin, J. W., Haynes, R. R., Roberts, V. L., & Alem, N. M. (1970). Material properties of cranial bone. *Journal of Biomechanics*, 3, 495–511.
- McIvor, I. K., & Sonstegard, D. A. (1966). Axisymmetric response of a closed spherical shell to a nearly uniform radial impulse. *The Journal of the Acoustical Society of America*, 40(6), 1540–1547.
- O'Neill, G., Summer, L., & Shirey, L. (1999). Hearing loss: A growing problem that affects quality of life. Tech. rep., National Academy on an Aging Society.
- Osten, W. (Ed.) (2007). *Optical Inspection of Microsystems*. Taylor & Francis Group, LLC.
- Polytec GmbH (2012). Polytec - advancing measurements by light.
URL <http://www.polytec.com/us/>
- Polytec GmbH (n.d.a). *Software Manual: Polytec Scanning Vibrometer Software 8.4*. Polytec GmbH.
- Polytec GmbH (n.d.b). *Theory Manual: Polytec Scanning Vibrometer*. Polytec GmbH.
- Sim, J. H., Chatzimichalis, M., Lauxmann, M., Rösli, C., Eiber, A., & Huber, A. M. (2010). Complex stapes motions in human ears. *Journal of the Association for Research in Otolaryngology*, 11, 329–341.

- Stenfelt, S., & Goode, R. (2005a). Bone-conducted sound: Physiological and clinical aspects. *Otology & Neurotology*, 26(6), 1245–1261.
- Stenfelt, S., & Goode, R. (2005b). Transmission properties of bone conducted sound: measurements in cadaver heads. *The Journal of the Acoustical Society of America*, 118(4), 2373–2391.
- Stenfelt, S., Håkansson, B., & Tjellström, A. (2000). Vibration characteristics of bone conducted sound in vitro. *The Journal of the Acoustical Society of America*, 107(1), 422–431.
- Stenfelt, S., Puria, S., Hato, N., & Goode, R. (2003). Basilar membrane and osseous spiral lamina motion in human cadavers with air and bone conduction stimuli. *Hearing Research*, 181, 131–143.
- Tjellström, A., Håkansson, B., & Granström, G. (2001). Bone-anchored hearing aids - current status in adults and children. *Otolaryngologic Clinics of North America*, 34(2).
- Tjellström, A., Rosenhall, U., Lindström, J., Hallén, O., Alberktsson, T., & Bråemark, P. I. (1983). Five-year experience with skin-penetrating bone-anchored implants in the temporal bone. *Acta Otolaryngol*, 95, 568–575.
- Tonndorf, J. (1966). Bone conduction: studies in experimental animals. *Acta Otolaryngol*, 213, 1–132.
- Tonndorf, J., & Jahn, A. F. (1981). Velocity of propagation of bone-conducted sound in a human head. *The Journal of the Acoustical Society of America*, 70(5), 1294–1297.
- Trnka, J., Veselý, E., & Dvořáková, P. (2004). A study of wave propagation in a human skull using laser interferometry. *Experimental Techniques*, 25(1), 27–30.
- von Békésy, G. (1955). Paradoxical direction of wave travel along the cochlear partition. *The Journal of the Acoustical Society of America*, 27(1), 137–145.
- Zwislocki, J. (1953). Acoustic attenuation between the ears. *The Journal of the Acoustical Society of America*, 25(4), 752–759.

APPENDIX A

FORCE AND ADMITTANCE

CALCULATION - MATLAB[®] CODE

The MATLAB[®] code that calculates the force and admittance of Skull A using data from Experiment 1. A similar code is used to calculate the force and admittance of Skull B.

Force Calculation

```
1 %% CALCULATE FORCE
2 % Force data computed using  $F = m * a$ 
3 %   F = force applied to abutment
4 %   m = mass of counter weight in Baha; fitting parameter ...
   determined from
5 %   LDV vs Simulator experiment (5.5 g)
6 %   a = acceleration data of Baha in z-direction
7
8 clear; clc;
9
10 %read in LDV force data
11 fid = fopen('Force Calc - Accel\baha_low_ref3.txt', 'r');
12 ForceData1 = textscan(fid, '%f %f %*f', 'headerlines', 5);
13 fclose(fid);
14
```



```

15 fid = fopen('Force Calc - Accel\baha_mid_ref3.txt', 'r');
16 ForceData2 = textscan(fid, '%f %f %*f', 'headerlines', 5);
17 fclose(fid);
18
19 fid = fopen('Force Calc - Accel\baha_high_ref3.txt', 'r');
20 ForceData3 = textscan(fid, '%f %f %*f', 'headerlines', 5);
21 fclose(fid);
22
23 fid = fopen('Force Calc - Accel\baha_low_vib.txt', 'r');
24 VibData1 = textscan(fid, '%*f %f %*f', 'headerlines', 5);
25 fclose(fid);
26
27 fid = fopen('Force Calc - Accel\baha_mid_vib.txt', 'r');
28 VibData2 = textscan(fid, '%*f %f %*f', 'headerlines', 5);
29 fclose(fid);
30
31 fid = fopen('Force Calc - Accel\baha_high_vib.txt', 'r');
32 VibData3 = textscan(fid, '%*f %f %*f', 'headerlines', 5);
33 fclose(fid);
34
35 %remove low frequencies (out of measured range)
36 i=1;
37 while ForceData1{1,1}(i,1) < 100
38     ForceData1{1,1}(i,:) = [];
39     ForceData1{1,2}(i,:) = [];
40     VibData1{1,1}(i,:) = [];
41 end
42
43 while ForceData2{1,1}(i,1) < 5500
44     ForceData2{1,1}(i,:) = [];
45     ForceData2{1,2}(i,:) = [];
46     VibData2{1,1}(i,:) = [];
47 end
48
49 while ForceData3{1,1}(i,1) < 10000
50     ForceData3{1,1}(i,:) = [];
51     ForceData3{1,2}(i,:) = [];
52     VibData3{1,1}(i,:) = [];
53 end

```

```

54
55 %remove high frequencies (out of measured range)
56 i = size(ForceData1{1,1},1);
57 while ForceData1{1,1}(i,1) ≥ 5500
58     ForceData1{1,1}(i,:) = [];
59     ForceData1{1,2}(i,:) = [];
60     VibData1{1,1}(i,:) = [];
61     i=size(ForceData1{1,1},1);
62 end
63
64 j = size(ForceData2{1,1},1);
65 while ForceData2{1,1}(j,1) ≥ 10000
66     ForceData2{1,1}(j,:) = [];
67     ForceData2{1,2}(j,:) = [];
68     VibData2{1,1}(j,:) = [];
69     j=size(ForceData2{1,1},1);
70 end
71
72 k = size(ForceData3{1,1},1);
73 while ForceData3{1,1}(k,1) > 20000
74     ForceData3{1,1}(k,:) = [];
75     ForceData3{1,2}(k,:) = [];
76     VibData3{1,1}(k,:) = [];
77     k=size(ForceData3{1,1},1);
78 end
79
80 Freq = [ForceData1{1,1};ForceData2{1,1};ForceData3{1,1}];
81 Accel = [ForceData1{1,2};ForceData2{1,2};ForceData3{1,2}];
82 Vib = [VibData1{1,1};VibData2{1,1};VibData3{1,1}];
83
84 %calculate force
85 m = 5.5 * 10 ^ (-3); %kg
86 TF_Accel = Accel - Vib; %0dB = m/s^2 / V
87 Accel_Linear = 10 .^ (TF_Accel ./ 20);
88 Force_Linear = m .* Accel_Linear;
89 %calculate force/voltage data for admittance calculation
90 Force = 20 .* log10(Force_Linear); %0dB = N / V
91
92 %plot force

```

```

93 figure
94 loglog(Freq,Force_Linear)
95 xhandle = xlabel('Frequency (Hz)','FontSize',11, 'FontWeight', 'bold');
96 yhandle = ylabel('Force/Voltage (N/V)','FontSize',11, 'FontWeight', ...
    'bold');
97 set(xhandle,'FontName', 'Calibri')
98 set(yhandle,'FontName', 'Calibri')
99 v = axis;
100 axis([100 20000 v(3) v(4)])
101
102 %write force/voltage data to file
103 fid = fopen('input_force_data.txt', 'wt');
104 headerlines1 = ['Force/Voltage Baha Input Data'];
105 headerlines2 = ['100 - 20000 Hz'];
106 headerlines3 = ['0dB = 1 N/V'];
107 headerlines4 = ['Frequency (Hz) Force/Voltage (dB)'];
108 Data = [Freq, Force];
109 fprintf(fid,'%s \n%s \n%s \n%s \n', headerlines1, headerlines2, ...
    headerlines3, headerlines4);
110 fprintf(fid,'%f \t %f\n', Data);
111 fclose(fid);

```

Admittance Calculation

```

1 %% FINAL PROCESSED DATA
2 % Inverse --> Root sum square --> Average
3 % X, Y, Z data
4 % 5 sites
5 % Full frequency range (100 - 20000 Hz)
6 % Force data calculated in "Final_Force.m" file
7 % Use 'input_force_data.txt'
8
9 clear; clc;
10
11 %read in files
12 %site data
13 freq_range = cellstr({'low';'mid';'high'});
14 for i = 1 : 5           %5 sites

```

```

15     for j = 1 : 3         %x,y,z
16         for k = 1 : 3     %frequency range
17             fid = fopen(sprintf('Site ...
                        %d\\site%d_%s_ref%d_H2.txt',i,i,freq_range{k},j));
18             eval(['Data = textscan(fid, '%f %f', 'headerlines', 5);']);
19             eval(['Site' num2str(i) '{j,k}(:,1) = Data{1,1};']);    ...
                        %frequency
20             eval(['Site' num2str(i) '{j,k}(:,2) = Data{1,2};']);    ...
                        %velocity
21             Data = 0;
22         end
23     end
24 end
25 Freq_Low(:,1) = Site1{1,1}(:,1);
26 Freq_Mid(:,1) = Site1{1,2}(:,1);
27 Freq_High(:,1) = Site1{1,3}(:,1);
28
29 %force data
30 fid = fopen('input_force_data.txt', 'r');
31 ForceData = textscan(fid, '%f %f', 'headerlines', 4);
32 fclose(fid);
33 Force(:,1) = ForceData{1,2};
34
35 %remove low frequency noise
36 i=1;
37 while Freq_Low(i,1) < 100
38     Freq_Low(i,:) = [];
39     for j = 1 : 5         %5 sites
40         for k = 1 : 3     %x,y,z
41             eval(['Site' num2str(j) '{k,1}(i,:) = [];']);
42         end
43     end
44 end
45
46 while Freq_Mid(i,1) < 5500
47     Freq_Mid(i,:) = [];
48     for j = 1 : 5
49         for k = 1 : 3
50             eval(['Site' num2str(j) '{k,2}(i,:) = [];']);

```

```
51         end
52     end
53 end
54
55 while Freq_High(i,1) < 10000
56     Freq_High(i,:) = [];
57     for j = 1 : 5
58         for k = 1 : 3
59             eval(['Site' num2str(j) '{k,3}(i,:) = [];']);
60         end
61     end
62 end
63
64 %remove high frequencies (out of measured range)
65 i=size(Freq_Low,1);
66 while Freq_Low(i,1) ≥ 5500
67     Freq_Low(i,:) = [];
68     for j = 1 : 5
69         for k = 1 : 3
70             eval(['Site' num2str(j) '{k,1}(i,:) = [];']);
71         end
72     end
73     i=size(Freq_Low,1);
74 end
75
76 i=size(Freq_Mid,1);
77 while Freq_Mid(i,1) ≥ 10000
78     Freq_Mid(i,:) = [];
79     for j = 1 : 5
80         for k = 1 : 3
81             eval(['Site' num2str(j) '{k,2}(i,:) = [];']);
82         end
83     end
84     i=size(Freq_Mid,1);
85 end
86
87 i=size(Freq_High,1);
88 while Freq_High(i,1) > 20000
89     Freq_High(i,:) = [];
```

```

90     for j = 1 : 5
91         for k = 1 : 3
92             eval(['Site' num2str(j) '{k,3}(i,:) = [];']);
93         end
94     end
95     i=size(Freq_High,1);
96 end
97
98 Freq = [Freq_Low;Freq_Mid;Freq_High];
99 for i = 1 : 5      %sites
100     for j = 1 : 3  %x,y,z
101         eval(['Site' num2str(i) '{j,1} = [Site' num2str(i) ...
102             '{j,1}(:,2);Site' num2str(i) '{j,2}(:,2);Site' ...
103             num2str(i) '{j,3}(:,2)];']);
104         eval(['Site' num2str(i) '{j,2} = [];']);
105         eval(['Site' num2str(i) '{j,3} = [];']);
106     end
107 end
108 %inverse, RSS, average
109 Average_Linear = zeros(size(Freq,1),1);
110 Average = zeros(size(Freq,1),1);
111 for i = 1 : 5
112     eval(['Site' num2str(i) '_RSS = zeros(size(Freq,1),1);']);
113 end
114 for i = 1 : size(Freq,1)
115     for j = 1 : 5      %sites
116         for k = 1 : 3  %x,y,z
117             eval(['Linear = 10 ^ (-Site' num2str(j) '{k,1}(i) / ...
118                 20);']); %convert x,y,z to linear
119             eval(['Site' num2str(j) '_RSS(i) = Site' num2str(j) ...
120                 '_RSS(i) + Linear ^ 2;']); %sum the squares of the ...
121                 linear terms
122             Linear = [];
123         end
124     end
125     eval(['Average_Linear(i) = Average_Linear(i) + sqrt(Site' ...
126         num2str(j) '_RSS(i));']); %root the sum of the squares ...
127         and add all sites together

```

```

122     end
123     Average(i) = 20 * log10((Average_Linear(i))/5) - Force(i);    ...
        %complete average of sites by dividing by 5 --> convert ...
        back to dB --> divide by force
124 end
125
126 while Freq_Low(size(Freq_Low,1),1) > 1000
127     Freq_Low(size(Freq_Low,1),:) = [];
128 end
129
130 % To save data to text file
131 % fid = fopen('skull1_admittance.txt', 'wt');
132 % headerlines1 = ['Skull 1 Admittance'];
133 % headerlines2 = ['100 - 20000 Hz'];
134 % headerlines3 = ['0dB = m/s / N'];
135 % headerlines4 = ['Frequency (Hz)  Admittance (dB)'];
136 % Data = [Freq, Average];
137 % fprintf(fid,'%s \n%s \n%s \n%s \n', headerlines1, headerlines2, ...
        headerlines3, headerlines4);
138 % fprintf(fid,'%f \t \t %f\n', Data);
139 % fclose(fid);
140
141 %plot FFT and indicate peaks
142 figure
143 loglog(Freq,Average,Freq_Low, 20 .* log10(1 ./ Freq_Low) + 20 * ...
        log10(1/(2 * pi() * 0.440)), 'r-.')
144 xhandle = xlabel('Frequency (Hz)', 'FontSize',11, 'FontWeight', 'bold');
145 yhandle = ylabel('Admittance (dB rel m/s / N)', 'FontSize',11, ...
        'FontWeight', 'bold');
146 lhandle = legend('Experiment #1 - Skull A', '440g Point Mass');
147 set(xhandle, 'FontName', 'Calibri')
148 set(yhandle, 'FontName', 'Calibri')
149 set(lhandle, 'FontSize',11, 'FontName', 'Calibri')
150 %title(['Magnitude Averaged over All 5 Experimental Sites on a Dry ...
        Human Skull'])
151 v = axis;
152 axis([100 20000 v(3) -10^1.5])

```

APPENDIX B

VISUAL BASIC[®] MACROS

Visual Basic[®] Macros were developed to automate processes in the PSV software.

Settings Macro

This macro loads an "original" settings file, changes the frequency and saves as a new settings files. The "original" settings file is generated manually in the PSV software prior to running this macro and contains the channel and acquisition settings for the desired frequency range. For this reason the channel and acquisition settings must be the same for all files generated as the macro will only change the frequency. The macro given here saves the first 11 settings files for the 41 frequency dataset obtained in Experiment 2. The remaining 30 settings files were generated by saving a new "original" settings file in the PSV software with the appropriate channel and acquisition settings for the high frequency range.

```
1 '#Uses "SwitchToAcquisitionMode.bas" '
2
3 Option Explicit
4
5 ' Original Settings File '
6 Const C_Settings = "Settings.set"
7
```



```
8 ' Path of Settings File
9 Const C_Path = "G:\Carmen\Skull 2\Settings\"
10
11
12 Sub Main
13 ' -----
14 '   Main procedure.
15 ' -----
16     If Not SwitchToAcquisitionMode() Then
17         MsgBox "Switch to acquisition mode failed."
18     End If
19 End If
20
21 Dim i As Integer
22 Dim sFile As String
23 Dim sNewFile As String
24 Dim Doc As Settings
25 sFile = C_Path + C_Settings
26
27 For i% = 0 To 11
28     Settings.Load(sFile, ptcSettingsAcquisition)
29     Dim Sine As New WaveformSine
30     Sine.Frequency=6000+(i)*350
31
32     Application.Acquisition.Mode =ptcAcqModeFft
33
34     Dim gen As GeneratorAcqProperties
35     Set gen = Application.Acquisition.ActiveProperties ...
36         .Item(ptcAcqPropertiesTypeGenerators)(1)
37     gen.Waveform=Sine
38
39     sNewFile="Settings" + CStr(i+6) + ".set"
40     Settings.Save(sNewFile)
41 Next i%
42
43 MsgBox("Macro has finished.", vbOkOnly)
44 End Sub
```

```

1 Attribute VB_Name = "SwitchToAcquisitionMode"
2 ' POLYTEC CODE MODULE
3 ' -----
4 ' PSV:      This code module switches the application to the
5 '           acquisition mode.
6 ' This code module cannot be executed directly, it is used by other
7 ' macros.
8 ' -----
9 '
10 ' Return values:
11 ' True: Application is in acquisition mode after execution
12 ' False: Application is in presentation mode after execution
13 '
14 Public Function SwitchToAcquisitionMode() As Boolean
15
16     If Application.Mode = ptcApplicationModeNormal Then
17         ' VibSoft is running, there is only one ApplicationMode
18         SwitchToAcquisitionMode = True
19     Else
20         ' PSV is running
21         If Application.Mode = ptcApplicationModePresentation Then
22             ' Switch to Acquisition Mode
23             Application.Mode = ptcApplicationModeAcquisition
24         End If
25
26         ' Check if Application is switched to Acquisition Mode
27         If Application.Mode = ptcApplicationModePresentation Then
28             Beep
29             MsgBox "Cannot switch to Acquisition Mode"
30             SwitchToAcquisitionMode = False
31         Else
32             SwitchToAcquisitionMode = True
33         End If
34     End If
35
36 End Function

```

Scan Macro

This macro loads settings files, either generated manually or using the settings macro, runs a full scan and saves the data in an *.svd file for each settings file. The macro given here acquires data for all frequencies in the 41 frequency dataset obtained in Experiment 2.

```

1 '#Uses "SwitchToAcquisitionMode.bas"
2
3 Option Explicit
4
5 ' Path with settings files
6 Const C_Path = "G:\Carmen\Skull 2\Settings\"
7
8 ' Directory for saving the scans
9 Const C_Directory = "G:\Carmen\Skull 2\BackView\ScanFiles\"
10
11 Sub Main
12 ' -----
13 '   Main procedure.
14 ' -----
15 '   Switch to Acquisition Mode
16   If Not SwitchToAcquisitionMode() Then
17       MsgBox "Switch to acquisition mode failed."
18       End
19   End If
20
21   Dim i As Integer
22   Dim freq As Double      ' Frequency
23   Dim sFile As String    ' Settings file
24   Dim sNewFile As String ' SVD file
25
26   For i% = 1 To 41
27
28       '   Load AD-settings and point definitions and camera
29       '   settings (note: use 'Or' to combine flags)
30       On Error GoTo SettingsNotAvailable
31       sFile = C_Path + "Settings" + CStr(i) + ".set"
32       Settings.Load sFile, ptcSettingsAcquisition Or ...

```

```

33         ptcSettingsAPS Or ptcSettingsCamera Or ptcSettingsWindows
34
35     On Error GoTo 0      ' Stop macro on Error
36
37     Dim gen As GeneratorAcqProperties
38
39     '         this sets the acquisition type to SINE                                     '
40     Set gen = Application.Acquisition.ActiveProperties ...
41         .Item(ptcAcqPropertiesTypeGenerators) (1)
42
43     '         Get frequency from settings file                                         '
44     Dim wave As WaveformSine
45
46     Set wave = gen.Waveform
47
48     freq = wave.Frequency
49
50     '         Start scan                                                               '
51     sNewFile=C_Directory + "SkullB.Posterior." + CStr(freq) ...
52         + "Hz" + ".svd"
53     Acquisition.ScanFileName = sNewFile
54     Acquisition.Scan ptcScanAll
55
56     '         Wait until scan finished                                               '
57     While Acquisition.State <> ptcAcqStateStopped
58         Wait 1
59     Wend
60
61     GoTo NoError
62
63 SettingsNotAvailable:
64     If Err.Number <> 0 Then
65         MsgBox "Settings " + "Settings" + CStr(i) + ".set" + ...
66             " not found."
67     End If
68
69 NoError:
70     Next i%
71

```

```

72     MsgBox("Macro has finished.", vbOkOnly)
73 End Sub

1  Attribute VB_Name = "SwitchToAcquisitionMode"
2  ' POLYTEC CODE MODULE
3  ' -----
4  ' PSV:      This code module switches the application to the
5  '           acquisition mode.
6  ' This code module cannot be executed directly, it is used by other
7  ' macros.
8  ' -----
9  '
10 ' Return values:
11 ' True: Application is in acquisition mode after execution
12 ' False: Application is in presentation mode after execution
13 '
14 Public Function SwitchToAcquisitionMode() As Boolean
15
16     If Application.Mode = ptcApplicationModeNormal Then
17         VibSoft is running, there is only one ApplicationMode
18         SwitchToAcquisitionMode = True
19     Else
20         PSV is running
21         If Application.Mode = ptcApplicationModePresentation Then
22             Switch to Acquisition Mode
23             Application.Mode = ptcApplicationModeAcquisition
24         End If
25
26         Check if Application is switched to Acquisition Mode
27         If Application.Mode = ptcApplicationModePresentation Then
28             Beep
29             MsgBox "Cannot switch to Acquisition Mode"
30             SwitchToAcquisitionMode = False
31         Else
32             SwitchToAcquisitionMode = True
33         End If
34     End If
35

```

36 End Function

APPENDIX C

EXPERIMENT 2 DATA ANALYSIS

The following is a detailed description of the data analysis performed by Dr. Robert B. Adamson in the S.E.N.S.E. Laboratory at Dalhousie University on the 41 frequency dataset acquired from Experiment 2.

In the posterior view encompassing the left parietal and occipital bones, the skull thickness and curvature were relatively uniform, and so it was felt that the wave number at a given frequency was most likely to be spatially uniform as compared to the other views. If the wave number was indeed spatially uniform over the measured region, then the dependence of wave number on frequency could be determined by extracting the wave number from the measured velocity field. The velocity fields at 41 different frequencies ranging from 6000 Hz to 20000 Hz at 350 Hz spacings were measured in this view. A 3D vectorial representation of the velocity field can be seen in Figure C.1 for a representative frequency, 10550 Hz. The velocity field is typified by regions where the velocity is normal to the surface surrounded by regions where the velocity vector is tangential to the surface and pointing towards the region of outward normal deflection. While characteristic of plate waves generally, such behaviour is common to flexural and extensional waves as well as to surface or Rayleigh waves, and so does not help to distinguish between them. It is therefore not possible to distinguish the different types of waves using this observation alone.

Figure C.2 shows the normal and tangential components of the velocity for an arc along the skull surface at a frequency of 10550 Hz. The tangential component of the velocity is taken

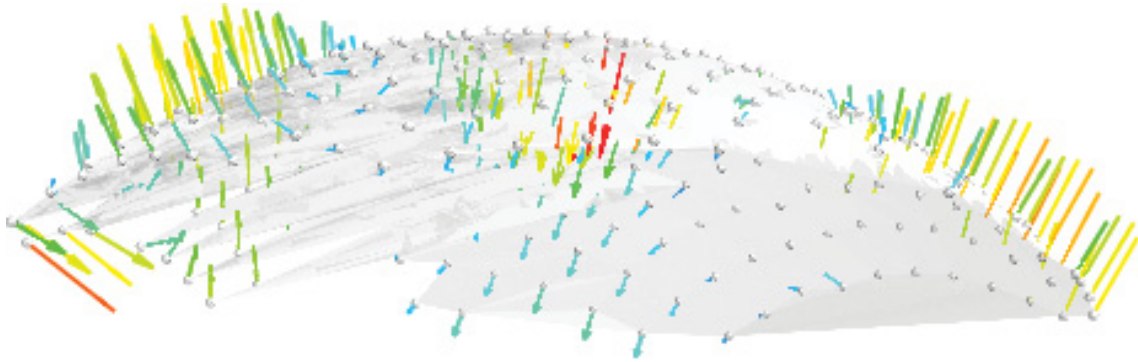


Figure C.1: Plot showing the 3D velocity field on the surface of the anterior portion of the skull. Arrows show the direction of surface motion and arrow length indicates the velocity magnitude

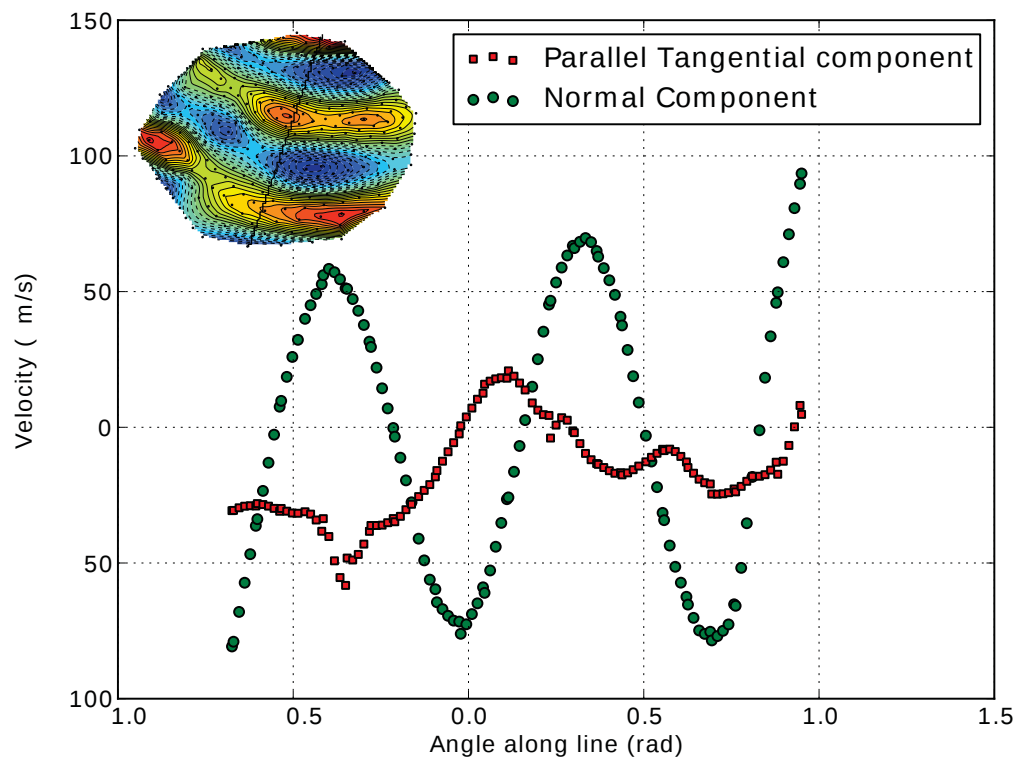


Figure C.2: Plot showing the normal and tangential components of the velocity vector along an arc on the surface roughly parallel to the wave vector with excitation at 10550 Hz. The tangential component of the velocity is the projection of the velocity vector along the arc and the normal component is the projection normal to the surface. The inset shows the arc on a 2D contour plot of normal velocity.

parallel to the arc, which, for this frequency, was a good approximation to the wave vector direction. While there are some additional components to the tangential velocity, it is clear that both the normal and tangential components exhibit roughly sinusoidal oscillation with angle and that the normal and tangential components are 90° out of phase with each other. Again, these are generic features of plate and surface waves and so do not help to distinguish them, but they do provide clear evidence for wavelike distortions at these frequencies.

In order to determine the dispersion relationship, the 3D grid points were projected onto a spherical surface obtained from a least-squares fit so that grid points could be identified by elevation and azimuthal angles. The RMS deviation from sphericity for grid points was 11% of the radius, so the spherical approximation was reasonable. The velocity vector was then projected onto the surface normal of the sphere at each point and the normal velocity plotted for each frequency. The measured data were linearly interpolated onto a finer grid created with the Delauney triangulation algorithm (using matplotlib's `griddata` function) and contours of the interpolated data were generated to aid visualization. The measured grid points are depicted by black circles in the plots. The tangential projection of the velocity at each grid point is depicted as a vector field overlaid on the plot. Figure C.3 shows the normal velocity over the surface at four representative frequencies, 6700 Hz, 10550 Hz, 15100 Hz and 19300 Hz.

Visual inspection of the velocity fields shows that at each frequency there is a characteristic length scale to variations in the patterns, indicating a wavelength that is reasonably constant over the measured surface. Furthermore, this length scale becomes noticeably shorter as the excitation frequency is increased. To obtain a quantitative estimate of this wavelength, the normal velocity field at each frequency was assumed to be a weighted sum of sine waves propagating from different directions but all having the same wave number (i.e. the same magnitude of the wave vector $k = |\vec{k}| = \frac{2\pi}{\lambda}$ where the units for k are inverse radians since the grid point coordinates are angles). The normal velocity amplitude V at each

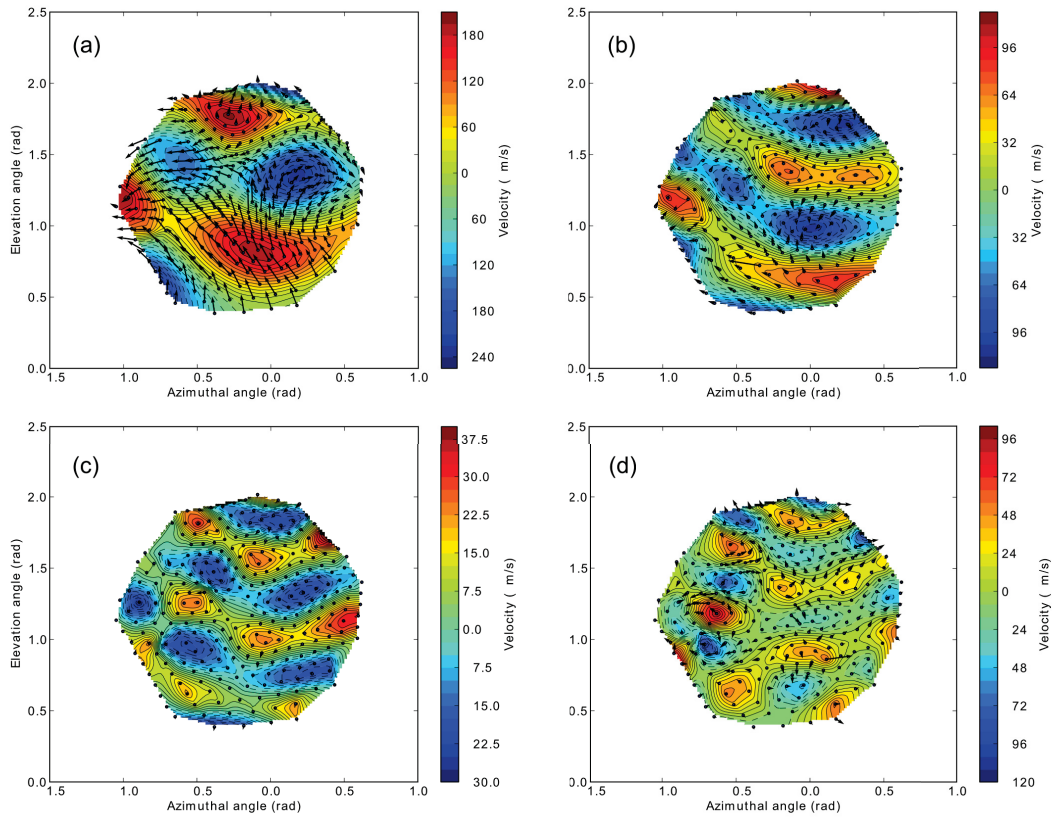


Figure C.3: Contour plots showing the normal component of the surface velocity as a function of angle for the projection of the skull surface onto a sphere at four representative frequencies (a) 6700 Hz, (b) 10550 Hz, (c) 15100 Hz and (d) 19300 Hz. The arrows on the surface show the direction and relative magnitude of the tangential component of the velocity.

frequency was expressed as

$$V(\theta, \phi) = \sum_{n=1}^N \left[A_n \cos \left(k(\omega) \left[\theta \cos \frac{2\pi n}{N} + \phi \sin \frac{2\pi n}{N} \right] \right) + \right. \quad (\text{C.1})$$

$$\left. B_n \sin \left(k(\omega) \left[\theta \cos \frac{2\pi n}{N} + \phi \sin \frac{2\pi n}{N} \right] \right) \right] \quad (\text{C.2})$$

where A_n and B_n are weighting constants, θ and ϕ are the two angular directions, N is the number of different directions being considered, and $k(\omega) = \frac{2\pi}{\lambda(\omega)}$ is the wave number of a wave of wavelength $\lambda(\omega)$ at frequency ω .

For a given wave number the constants A_i and B_i can be obtained from the normal velocity

field by making use of orthonormality of the sine and cosine functions,

$$A_n = \iint_{\Omega} V(\theta, \phi) \cos \left[k \left(\theta \cos \frac{2\pi n}{N} + \phi \sin \frac{2\pi n}{N} \right) \right] d\Omega \quad (\text{C.3})$$

$$B_n = \iint_{\Omega} V(\theta, \phi) \sin \left[k \left(\theta \cos \frac{2\pi n}{N} + \phi \sin \frac{2\pi n}{N} \right) \right] d\Omega \quad (\text{C.4})$$

A numerical optimization routine was used to select the value of k that provided the best estimate of the velocity field for each frequency. The optimization made use of the `numpy` implementation of Brent's method for root-finding on a bounded interval (Brent, 1973).

APPENDIX D

CONSTRAINED, NON-LINEAR LEAST SQUARES OPTIMIZATION SCHEME

The MATLAB[®] code used to perform a constrained, non-linear least squares optimization to determine the geometric and material parameters that best fit a spherical shell model to the dispersion relationship in the skull. The parameters were varied within reasonable limits for human skull bone.

```
1 clc; clear;
2 % Skull 1
3 % starting guesses
4 E0 = 7 * 10 ^ 9;
5 ro0 = 1820;
6 nu0 = 0.3;
7 h0 = 0.0065;
8
9 x0 = [E0 ro0 nu0 h0];
10
11 % optimization
12 options = optimset('Disp','iter');
13 [x,resnorm,F] = lsqnonlin(@myfun1,x0,[3*10^9 1000 0.15 ...
    5*10^(-3)], [8*10^9 2000 0.33 9*10^(-3)],options);
14
15 % plot optimization
16 a = 0.072;          % mean radius (m) for Skull 1 from shell fit
```

```

17 n = [1:1:20];      % mode number
18 lambda = n .* (n + 1);
19
20 % read in experimental data
21 file = fopen('skull1_freqs_and_m.txt');
22 data = textscan(file, '%f %f');
23 fclose(file);
24
25 % experimental data calculations
26 freq_exp(:,1) = data{1,1};
27 mode_exp(:,1) = data{1,2};
28 cp = sqrt(x(1) / (x(2) * (1 - x(3)^2)));
29 omega_exp = 2 .* pi() .* freq_exp .* a ./ cp;
30
31 % model
32 beta_sq = x(4) ^ 2 / (12 * a ^ 2);
33 lambda = n .* (n + 1);
34 c1 = 1 + 3 * x(3) + lambda - beta_sq * (1 - x(3) - lambda .^ 2 - ...
      x(3) .* lambda);
35 c2 = (lambda - 2) .* (1 - x(3) ^ 2) + beta_sq * (lambda .^ 3 - 4 .* ...
      lambda .^ 2 + lambda .* (5 - x(3) ^ 2) - 2 * (1 - x(3) ^ 2));
36 omega_model = sqrt((c1 - sqrt(c1 .^ 2 - 4 .* c2)) ./ 2);
37
38 % plotting
39 figure
40 plot(mode_exp,omega_exp,'r',n,omega_model,'b')
41 xhandle = xlabel('Mode Number','FontSize',11, 'FontWeight', 'bold');
42 yhandle = ylabel('Frequency (Hz)','FontSize',11, 'FontWeight', 'bold');
43 lhandle = legend('Experiment 2 Results - Skull A','Spherical Shell ...
      Model - Lower Branch','Location','NorthWest'); %
44 set(xhandle,'FontName', 'Calibri')
45 set(yhandle,'FontName', 'Calibri')
46 set(lhandle,'FontSize',11,'FontName', 'Calibri')
47
48
49 function F = myfun1(x)
50 %Skull 1
51 a = 0.072;      % radius of curvature
52

```

```

53 % read in experimental data
54 file = fopen('skull1_freqs_and_m.txt');
55 data = textscan(file, '%f %f');
56 fclose(file);
57
58 % experimental data calculations
59 freq_exp(:,1) = data{1,1};
60 mode_exp(:,1) = data{1,2};
61 cp = sqrt(x(1) / (x(2) * (1 - x(3)^2)));
62 omega_exp = 2 .* pi() .* freq_exp .* a ./ cp;
63
64 % model
65 beta_sq = x(4) ^ 2 / (12 * a ^ 2);
66 lambda = mode_exp .* (mode_exp + 1);
67 c1 = 1 + 3 * x(3) + lambda - beta_sq * (1 - x(3) - lambda .^ 2 - ...
    x(3) .* lambda);
68 c2 = (lambda - 2) .* (1 - x(3) ^ 2) + beta_sq * (lambda .^ 3 - 4 .* ...
    lambda .^ 2 + lambda .* (5 - x(3) ^ 2) - 2 * (1 - x(3) ^ 2));
69 omega_model = sqrt((c1 - sqrt(c1 .^ 2 - 4 .* c2)) ./ 2);
70
71 %optimization
72 F = omega_exp - omega_model;

```